# Diversity of 3D APAR and LAI dynamics in broadleaf and coniferous forests: Implications for the interpretation of remote sensing-based products

Kesselring, Jasmin ; Morsdorf, Felix ; Kükenbrink, Daniel ; Gastellu-Etchegorry, Jean-Philippe ; Damm, Alexander

DOI: https://doi.org/10.1016/j.rse.2024.114116

Remote Sensing of Environment 306 (2024) 114116

Contents lists available at ScienceDirect

Remote Sensing of Environment

journal homepage: www.elsevier.com/locate/rse

# Diversity of 3D APAR and LAI dynamics in broadleaf and coniferous forests: Implications for the interpretation of remote sensing-based products

Jasmin Kesselring [a,*], Felix Morsdorf [a,b], Daniel Kükenbrink [b], Jean-Philippe Gastellu-Etchegorry [c], Alexander Damm [a,d]

[a] Department of Geography, University of Zurich, 8057 Zürich, Switzerland
[b] Swiss Federal Institute for Forest, Snow and Landscape Research WSL, Zürcherstrasse 111, 8903 Birmensdorf, Switzerland
[c] Centre d'Etudes Spatiales de la BIOsphère (CESBIO), Toulouse University (UPS, CNES, CNRS, IRD), 31401 Toulouse, France
[d] Eawag, Swiss Federal Institute of Aquatic Science and Technology, 8600 Dübendorf, Switzerland

ARTICLE INFO

Edited by: Jing M. Chen

*Keywords:*
Radiative transfer modeling
DART
3D virtual scenes
Forest ecosystems
Illumination effects
Shadow

ABSTRACT

Forests substantially mediate the water and carbon dioxide exchanges between terrestrial ecosystems and the atmosphere. The rate of this exchange, including evapotranspiration (ET) and gross primary production (GPP), depends mainly on the underlying vegetation type, health state, and the composition of abiotic environmental drivers. However, the complex 3D structure of forest canopies and the inherent top-view perspective of optical and thermal remote sensing complicate remote sensing-based retrievals of biotic and abiotic factors that eventually determine ET and GPP. This study investigates the sensitivity of remote sensing approaches to 3D variation of abiotic and biotic environmental drivers. We use 3D virtual scenes of two structurally different Swiss forests and the radiative transfer model DART to simulate the 3D distribution of solar irradiance and reflected radiance in the forest canopy. These simulations, in combination with LiDAR data, are used to derive the absorbed photosynthetic active radiation (APAR) and the leaf area index (LAI) in 3D space. The 3D variation of both parameters was quantified and analyzed. We then simulated images of the top-of-canopy bi-directional reflectance factor (BRF) and compared them with the hemispheric-conical reflectance factor (HCRF) data derived from HyPlant airborne imaging spectrometer measurements. The simulated BRF data was used to derive APAR and LAI, and the results were compared to their respective 3D representations. We unravel considerable spatial differences between both representations. We discuss possible reasons for the disagreement, including a potential insensitivity of the inherent top-of-canopy view for the real 3D product dynamics and limitations of the processing of remote sensing data, especially the approximation of effective surface irradiance. Our results can help understanding sources of uncertainties in remote sensing based gas exchange products and defining mitigation strategies.

## 1. Introduction

Vegetation mediates the exchange of water and carbon dioxide ($CO_2$) with the atmosphere through transpiration and photosynthesis. The rate of this gas exchange depends on numerous biotic and abiotic variables specific to the underlying vegetation composition and ecosystem (Etzold et al., 2011; Tenhunen et al., 1998). Climate change caused temporal and spatial variation of abiotic factors, including temperature and precipitation, can enhance the naturally occurring variability of gas exchange processes in forests (Baldocchi et al., 2002; Fisher et al., 2017). Detailed assessments of forest carbon and water exchange are vital to understanding and quantifying the consequences of climate change on these abundant and valuable ecosystems (Hatfield and Dold, 2019; Mkaouar et al., 2021).

The 3D spatial heterogeneity of forest canopies challenges the assessment of ecosystem gross primary production (GPP) and evapotranspiration (ET) (Lin et al., 2018; Paul-Limoges et al., 2020; Staudt et al., 2011). Notably, the dependence of both exchange processes on vegetation state and type and the composition of abiotic environmental drivers causes large horizontal and vertical variability that must be appropriately resolved in observational and model-based assessments. Added complexity comes from the fact that leaves at the top of the

* Corresponding author.
*E-mail address:* jasmin.kesselring@geo.uzh.ch (J. Kesselring).

https://doi.org/10.1016/j.rse.2024.114116
Received 7 August 2023; Received in revised form 8 March 2024; Accepted 11 March 2024
Available online 26 March 2024

canopy are exposed to harsher conditions (i.e., high solar radiation, wind, temperature). This circumstance determines specific biochemical (e.g., pigments, water content), structural (e.g., size and shape), and functional (e.g., transpiration) differences of such exposed leaves compared to those protected in the canopy (Grzesiak et al., 2010; Hagemeier and Leuschner, 2019). Consequently, the assumption that the whole canopy has leaf properties similar to those at the top layer is incorrect. Further, solar radiation, temperature, and wind profiles largely depend on the vertical canopy structure and partly the biochemical and functional state of leaves (Baldocchi et al., 2002).

Modeling approaches allow accounting for this 3D spatial variation at different levels of complexity (Wang and Frankenberg, 2022), ranging from relatively simple big-leaf to multilayer canopy approximations (Bonan et al., 2021), with varying estimates of GPP or ET depending on the implementation (Sprintsin et al., 2012; Zhang et al., 2016). In situ observations required for the parameterization, calibration, and validation of modeling approaches also allow vertically stratified assessments. In particular, the eddy covariance technique is an established technique to estimate forest abiotic factors and gas exchange on a local scale (Baldocchi et al., 2001). At several sites, sensors are vertically distributed in the ecosystem to measure variations of atmospheric $CO_2$ and water vapor as proxies for gas exchange on a canopy scale (Baldocchi, 2003). Remote sensing (RS) is a proven alternative to provide information about the horizontal dynamic of abiotic and biotic factors to estimate vegetation gas exchange across spatial scales (Paul-Limoges et al., 2018). In fact, airborne and satellite-based approaches were successfully applied to quantify GPP (Braun et al., 2017; Chen et al., 2022; Junttila et al., 2023) and ET (Anderson et al., 2012; Burchard-Levine et al., 2021; Running et al., 2019) by implicitly following the big-leaf paradigm. Despite the valuable insight provided by past studies, the latest knowledge derived from spatial high-resolution data and simulation experiments (Damm et al., 2020) increased our understanding of additional challenges that must be tackled to overcome the inherent limitations of RS and advance the reliability of RS-based estimates of GPP and ET.

One notable challenge is the inherent top-view perspective of airborne and satellite RS that limits the sensitivity of optical and thermal observations for the vertical distribution of abiotic and biotic factors in vegetation canopies (Elsherif et al., 2019). It is obvious that leaves of the outer canopy are exposed to more harsh environmental conditions and are mostly visible by RS sensors. How vegetation information and environmental factors derived from such an RS perspective represent the vertical dynamics of these factors across forest types is largely unknown (Damm et al., 2020). Another challenge relates to the preprocessing of RS data. Particularly, the retrieval of reflectance is subject to uncertainty caused by the assumption that all pixels in a forest canopy are fully illuminated. For high resolution data, geometric optical scattering causes shadows that complicate the description of the radiative transfer (Fawcett et al., 2018) and can cause uncertainties in reflectance data and subsequently derived products (Kükenbrink et al., 2019). The assessment of uncertainties in retrieved vegetation information and environmental factors caused by data processing is understudied.

This study aims to quantify the sensitivity and reliability of RS-derived vegetation information considering i) 3D canopy variation and ii) the effects of shading in two structurally different forest ecosystems. We construct 3D virtual scenes of two contrasting forests in Switzerland (i.e., a temperate mixed deciduous forest and an alpine coniferous forest) using both LiDAR and in situ spectroscopy data. We focus on two environmental factors that largely drive vegetation gas exchange: i) absorbed photosynthetic active radiation (APAR) as a highly dynamic factor largely determined by illumination angles, atmospheric properties, and canopy structure, and ii) the leaf area index (LAI) as a less dynamic factor representing canopy structure. The distribution of both factors was modeled in 3D using the LiDAR-derived forest structure and the radiative transfer model DART (Discrete Anisotropic Radiative Transfer) (Gastellu-Etchegorry et al., 2015). The 3D representation is then compared and contrasted with simulated top-of-canopy RS representations. We finalize our assessment by comparing the simulated bi-directional reflectance with measured airborne imaging spectroscopy data. We conclude on the challenges of representing complex ecosystem processes and underlying factors like LAI and APAR via RS measurements and indicate mitigation strategies.

## 2. Materials and methods

### 2.1. Study areas

Our analysis includes study sites of 50 m × 60 m in two structurally different forest types in two contrasting climatic regions in Switzerland. The Seehornwald in Davos (Fig. 1, top row) is a coniferous forest located in the Eastern Swiss Alps (46° 48′ 55.2″ N 9° 51′ 21.3″ E) at an elevation of 1639 m a.s.l. The site is dominated by Norway spruce, with an average canopy height of approximately 25 m (Etzold et al., 2011). The Laegern forest (Fig. 1, bottom row) is situated on a south-facing slope northwest of the city of Zurich (47° 28′ 40.8” N 8° 21′ 55.2″ E) at an elevation of 682 m a.s.l. (Paul-Limoges et al., 2018). It is a mixed deciduous forest dominated by beech trees with an average canopy height of 30.6 m (Etzold et al., 2011).

### 2.2. Data

#### 2.2.1. Airborne imagery

Airborne imaging spectroscopy data acquired with the HyPlant DUAL sensor on 15th June 2021 was used to validate the DART simulated top-of-canopy reflectance at both study sites. The HyPlant sensor system was developed by the Forschungszentrum Jülich in 2012. Used DUAL data cover the 380-2500 nm wavelength range with a spectral resolution of 3.65 nm in the visible to near infrared and 10.55 nm in the shortwave infrared (Siegmann et al., 2021). After acquiring the data, the software CaliGeoPro was used for the radiometric and geometric correction, and ATCOR-4 for the atmospheric correction (Siegmann et al., 2019). This project used a mosaic of corrected top-of-canopy reflectance data. Detailed data acquisition information for both study sites can be found in Table 1.

#### 2.2.2. LiDAR data acquisition and processing

The terrestrial LiDAR data in the coniferous forest was acquired in June 2021 using a Leica blk360 terrestrial laser scanner (TLS). For the deciduous forest, two existing data sets were used: i) A TLS point cloud acquired with a Leica blk360 in 2018 in leaf-on condition was used for the stem extraction. ii) The data set for the plant area density combines both TLS scans from a Riegl VZ-1000 and a UAV LiDAR system consisting of a RIEGL VUX-1UAV laser scanner mounted on the industrial Scout B1–100 UAV helicopter measured in 2017 (leaf-on) (for the acquisition and processing of the UAV data see Morsdorf et al. (2017)). The resulting LiDAR point clouds are used to generate the 3D virtual scenes. In this process, tree stem and foliage points need to be separated. The separation was achieved using a sequence of empirically optimized working steps to yield the best results for both forest types. First, the geometrical feature “verticality” (Hackel et al., 2016) was computed with a local neighborhood radius of 0.1. After filtering elements with verticality smaller than 0.9 for the coniferous and 0.6 in the deciduous forest, one is left with only the vertical elements in the point cloud. Second, the remaining foliage was removed using filters and thresholds. The noise filter (with neighborhood radius of 0.02) removed isolated points, and the result was further improved by applying a statistical outlier removal filter (30 neighboring points). As the last filter step, the point number per 5 cm voxel was used, assuming the point number is higher on tree stems than on the foliage. When inspecting visually, a threshold of 5 points per voxel for the coniferous and 10 points per voxel for the deciduous forests yielded the best results. Third, the RANSAC shape detection algorithm (Schnabel et al., 2007) using only cylinder


**Fig. 1.** Top row: coniferous forest site in Davos. Bottom row: deciduous forest site at Laegern. From left to right: top of canopy view true-color composite (RGB 640/550/460 nm) of the HyPlant airborne sensor with the study area marked as black square and the position of the eddy flux towers in blue; near canopy view as seen from the eddy flux tower platforms at the respective sites; vertical structure as seen from the forest floor. (For interpretation of the references to color in this figure legend, the reader is referred to the web version of this article.)

**Table 1**
Acquisition details of the used HyPlant images over both study sites.

| Parameter | Coniferous forest | Deciduous forest |
|---|---|---|
| No. of flight lines | 2 | 5 |
| Acquisition time [local] | 13:04–13:09 | 13:49–14:21 |
| Solar zenith [deg] | 23.6–23.7 | 24.6–26.6 |
| Solar azimuth [deg] | 171.1–173.6 | 193–209.7 |
| Flight height [m] | 1200 | 1800 |
| Pixel size [m] | 1.75 × 1.75 | 3 × 3 |

and cone shapes allowed the separation of the tree stem entities from the remaining point cloud (for parameter selection, see Table A1). After the semi-automatic separation of the point clouds, clear outliers were removed by hand in a final separation step. Poisson surface reconstruction transformed the remaining tree stem points into object elements (Kazhdan and Hoppe, 2013). The processing was done with R (v4.0.5) using the packages TreeLS (de Conto et al., 2017) and lidR (Roussel et al., 2020) and the point cloud tool CloudCompare (CloudCompare, 2021) with the PoissonRecon plugin (Kazhdan, 2021). The plant area density was calculated from the original point cloud (including all the wood elements) using the software AMAPVox (v1.8.1) (Vincent et al., 2017). In AMAPVox, the plant area density per voxel is derived from the optical density of a related cell of the gridded point cloud (de Boissieu et al., 2023; Kükenbrink et al., 2019). In detail, laser pulses are traced through the gridded point cloud to the last recorded hit. With the laser beam direction and distance, the software can calculate the local transmittance in each 3D cell the beam passes and infer the local plant area density (Nunes et al., 2022). The previously derived wood elements were subtracted to obtain the leaf area density. Because a complete separation between leaves and wood is difficult, we use the term estimated leaf area density (LAD*) for this product to indicate that small wood elements could still be present. The estimated leaf area index (LAI*) in 3D space was calculated by multiplying the LAD* per voxel by the voxel height (0.25 m). We defined the top-of-canopy LAI* representation as the cumulated LAI* values per voxel column.

#### 2.2.3. Leaf and ground spectroscopy data

The reflectance of tree bark, understory, and ground in the coniferous forest was measured with an ASD FieldSpec 3 field spectrometer on 15th June 2021 between 12:30 and 14:55. The bark of three different spruce trees was measured, two directly on the tree and one on the ground from a recently harvested tree. Spectra of the understory vegetation of mosses, blueberries, and Spruce cones were acquired in multiple suitable locations (i.e., randomly distributed with no shadow due to large trees) in the study plot and used as ground optical property. Measured radiance and irradiance (via a Spectralon white reference panel) were used to calculate surface reflectance. The retrieved reflectance spectra were post-processed to remove two well-known artifacts in the overlapping region of the three detectors caused by the different fields of view of the detectors and to reduce noise for low signal intensities, particularly in the short-wave infrared. The pre-processed single spectra were mixed into one bark and one ground spectrum. The weighting of each single measured spectrum in the overall spectrum is proportional to the occurrence on the study site, which was assessed by visual inspection of the site. All three bark spectra were assigned the same weight, and the ground spectrum consists of 49% blueberry, 49% moss, and 2% Spruce cones. The leaf and needle optical properties (LOP), for simplicity both are called LOP here, include reflectance and transmittance measurements. At the coniferous site, the LOP were measured with an SVC spectroradiometer and the corresponding integrating sphere on 8th September 2021 between 10:50 and 16:20 local time. Five Norway spruce trees were sampled at a height of 6 m. Access to the upper crown was not possible. The collected needles were taped to a 3D-printed sample holder. From each needle sample, reflectance and

**Table 2**
Threshold values were used to classify the 795–810 nm simulated bi-directional reflectance images into shaded, mixed, and illuminated pixels. Values are in the unit of reflectance for both the original DART resolution (0.25 m) and the convolved to HyPlant resolution (1.75 and 3.0 m) images across both forest sites.

| Threshold value [reflectance] | Coniferous forest | | | Deciduous forest | | |
|---|---|---|---|---|---|---|
| | Shaded | Mixed | Illum. | Shaded | Mixed | Illum. |
| Original DART resolution | < 4% | 4–29.5% | > 29.5% | < 15% | 15–52% | > 52% |
| Convolved to HyPlant resolution | < 5% | 5–29.5% | > 29.5% | < 20% | 20–45% | > 45% |

transmittance for three needle age groups were measured four times to cover biophysical traits variation that can vary strongly depending on age (Lhotáková et al., 2021), making it a total of 24 reflectance and 24 transmittance measurements per selected tree. The ratio between the needle area and the whole field-of-view area was extracted from photos of the samples by hand masking the needles (using Affinity Photo). This area ratio was then used to correct the too low reflectance and too high transmittance values, respectively, due to the gaps between the needles. At the deciduous site, no optical field measurements were made as the canopy is very dense, and access to the upper crowns was not possible. However, predefined spectra from the DART spectral library for the three optical categories mixed deciduous leaves, deciduous bark, and litter were used for the model. Even if the LOP are an important component of the radiative transfer simulation, Kükenbrink et al. (2021) showed that the canopy structure impacts the results to a much higher degree. For this reason, we devoted most of our resources to honing the structural representation of the two forest sites.

## 2.3. Methods

### 2.3.1. Construction of 3D virtual scenes

The Discrete Anisotropic Radiative Transfer model (DART) (Gastellu-Etchegorry et al., 2015) was used to simulate radiation interaction in the 3D vegetation canopies, including irradiance, radiance, and the radiative budget (RB) (i.e., voxel-wise absorbed, scattered, and transmitted radiance fraction) and subsequent data products such as APAR or RS-based bi-directional reflectance factors (BRF). DART was benchmarked in the RAMI4 model comparison and shown to result in comparable simulations of canopy optical properties (Widlowski et al., 2015). We use a voxel-based approach to generate the two 3D virtual scenes in the DART-FT (flux-tracking) (v.5.8.1) mode. The voxel size was set to 0.25 × 0.25 × 0.25 m. For the parameterization of the voxels, we followed the approach by Kükenbrink et al. (2019). The plant area density per voxel was directly derived from LiDAR data using the AMAPVox software. Concerning the LOP, it is known that the needle fraction per age class varies with height (Malenovský et al., 2008). However, since we did not have samples from different heights, we assumed a homogeneous mixture of measured LOP for all voxels representing trees. The leaf inclination distribution function (LIDF) was assumed to be spherical for the Norway Spruce trees (Janoutová et al., 2019; Schneider et al., 2014). For the broadleaf forest, a plagiophile distribution has been selected (Damm et al., 2020; Schneider et al., 2014). The topography of the resulting 3D scene was normalized using a digital elevation model generated from the TLS data using the R package lidR (Roussel et al., 2020). The terrain normalization comes at the cost of a more realistic representation of the simulated forest and may introduce artifacts due to the absence of topographical features. As both study sites are situated in flatter parts of the respective mountainous forests, introduced artifacts were minimal. Due to the normalization, further processing and interpretation are more straightforward, and the results are still comparable to the airborne spectroscopy data.

### 2.3.2. Simulation of airborne imagery

We used the virtual scene and simulated top-of-canopy airborne RS-based BRF images with DART to quantify the differences between 3D LAI and APAR dynamics and their RS-based representations. The BRF simulation considered HyPlant sensor characteristics and an illumination-observation geometry to represent the conditions during HyPlant data acquisition (Table 1). Atmospheric effects were considered using the middle latitude summer gas model (MIDLATSUM) and a rural aerosol concentration with 23 km visibility (USSTD76_RURALV23) for both sites. We reduced the number of simulated spectral bands to ten: one broadband 400–700 nm for the PAR region and nine narrower bands from the green to near-infrared (i.e., 528–532 nm, 547–554 nm, 569–573 nm, 644–679 nm, 667–674 nm, 795–810 nm, 797–804 nm, 890–905 nm, and 955–970 nm) (cf. also Fig. 3 for band visualization). The isolated scene mode was selected because there was no information on the forest geometry outside the 50 m × 60 m research plot. This increased the realism of the simulation scene boundaries as no artificial shadow of non-existing trees was added to the scene (important at the coniferous site as the plot borders a gravel road). For the convolution of the 0.25 m DART image to the respective HyPlant resolution, bigger kernel sizes (9 × 9 DART pixels for the coniferous and 15 × 15 for the deciduous forest) were combined via a weighted mean to simulate a HyPlant DUAL pixel (Siegmann et al., 2019). The resulting BRF images were compared against the HCRF data derived from HyPlant airborne measurements to check if the simulated BRF data are in a realistic value range.

### 2.3.3. Calculation of APAR and LAI from simulated remote sensing data

APAR and LAI are only calculated from DART-simulated BRF data, not the airborne HCRF data. This allows a pixel-wise comparison between simulated 3D and top-of-canopy view representations without introducing uncertainty by the co-registration with real airborne RS data. APAR is defined as the absorbed energy in the 400–700 nm wavelength region and is essential in determining gross primary production (Wei et al., 2017) and transpiration (Damm et al., 2020). Therefore, a broadband channel (400-700 nm) was simulated as radiative budget in DART to derive the 3D APAR information. Multiple approaches were tested for calculating APAR with simulated remote sensing images, but the method of Liu et al. (2004) resulted in the most consistent values compared to the 3D simulated data. This method estimates APAR (Eq. (2)) by multiplying the modified triangular vegetation index 2 (MTVI2, Eq. (1), initially introduced by Haboudane et al. (2004)) with the incident PAR.

$$MTVI2 = \frac{1.5[1.2(R_{800} - R_{550}) - 2.5(R_{670} - R_{550})]}{\sqrt{(2R_{800} + 1)^2 - (6R_{800} - 5\sqrt{R_{670}}) - 0.5}} \quad (1)$$

$$APAR = MTVI2 \bullet PAR \quad (2)$$

The reflectance at specific wavelengths ($R_x$) as used in Eq. (1) was approximated by the DART simulated narrow bands (see above). The incident PAR was calculated using the ratio of the radiance and

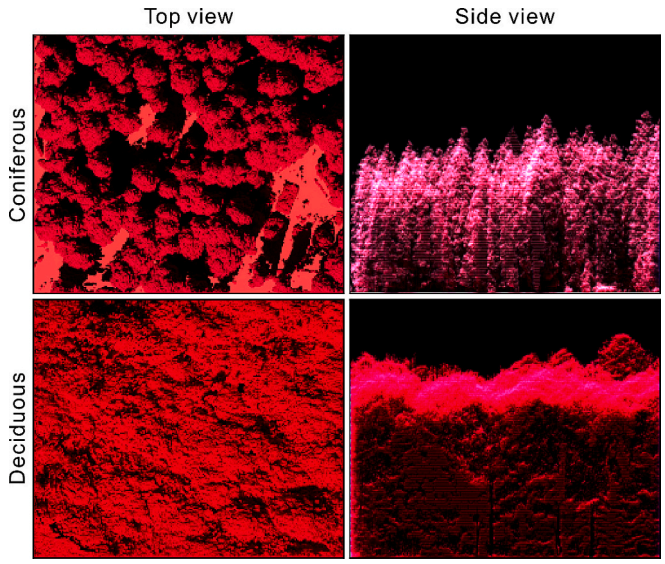


**Fig. 2.** False color infrared composite of the broadband bi-directional reflectance factor (BRF, left) and radiative budget (RB) averaged over the entire horizontal extent of the scene as side view (right) using DART-FT (RGB 802.5/672.5/550.5 nm) after applying a 5% linear contrast stretch for all bands. North is at the top of the top view images. The side view is shown in south-north direction, with the sun at an azimuth angle of 171° (coniferous) and 168° (deciduous). The top row shows the sub-alpine Norway Spruce forest in Davos, and the bottom row the temperate mixed forest Laegern.

reflectance of the simulated TOC image, resulting in a constant value over the whole scene (coniferous: 453 W/m$^2$, deciduous: 444 W/m$^2$). The LAI was approximated using the known relationship with the MTVI2 spectral index described in Haboudane et al. (2004) (Eq. (3)). For a visual overview of all data and methods used, see Fig. A1 in the Appendix.

$$LAI = 0.2227e^{3.6566MTVI2} \quad (3)$$

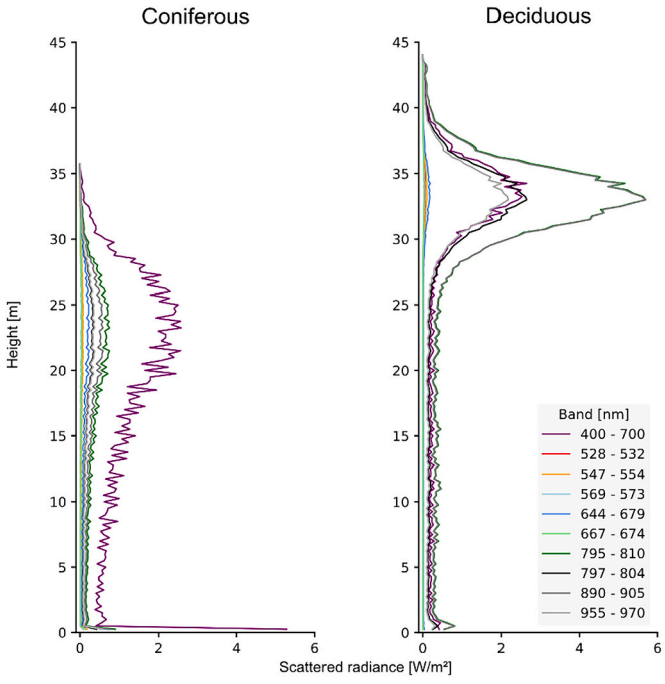


**Fig. 3.** DART-FT simulated vertical distribution of scattered radiance in all directions in ten spectral bands represented as the mean of the scattered radiance per voxel layer. The total height of the simulated canopies is 35.75 m for the coniferous forest and 44 m for the deciduous forest.

#### 2.3.4. Illumination classification

The simulated BRF images were classified according to their brightness into shaded, mixed, and illuminated pixels to analyze the calculated LAI and APAR maps in more detail (cf. Appendix Fig. A6 for the classified images). As shadows are more dominant in the near infrared (Rufenacht et al., 2013), we used multiple thresholds (Table 2) on the simulated 795–810 nm band in both the original DART resolution and convolved images to classify the pixels.

## 3. Results

### 3.1. 3D distribution of DART simulated radiance fields in both forest sites

3D virtual scenes were used to simulate the BRF and the RB with DART-FT for both forest sites. The BRF image is a top-of-canopy representation of the scene as observed by a RS sensor (Fig. 2 left) and was simulated for comparison with an real RS-derived reflectance product. The RB allows tracking different radiation components, including scattered and absorbed radiation per voxel (Fig. 2 right).

In the coniferous forest, some of the individual tree crowns can be distinguished from the top view, whereas the deciduous forest canopy is closed and more homogeneous. This is also reflected in the side view (Fig. 2), with recognizable tree crowns in the coniferous forest but a closed canopy layer in the deciduous forest. A vertical profile of the scattered radiance for the ten simulated spectral bands is shown in Fig. 3. The scattered radiance represents the amount of light scattered in all directions in the respective band. The values are generally higher in the upper tree crowns of the deciduous forest (up to 5.75 W/m$^2$ in the NIR band [797–804 nm]) compared to the coniferous forest (up to 0.75 W/m$^2$ in the NIR band). In contrast, the scattered radiance is vertically more evenly distributed in the coniferous forest compared to the rapid decrease after roughly 30 m height in the deciduous forest. As expected, light in longer wavelengths is scattered more than in shorter wavelengths.

### 3.2. 3D distribution of simulated LAI* and APAR across forest sites

The horizontal and vertical distribution of LAI* across both forest sites is shown in Fig. 4 and indicates large differences. Coniferous trees have the highest LAI* in the middle of the tree, with a conical decrease to the edge of the tree. Some larger trees can be recognized in the deciduous forest since they have a higher LAI* in a rounded pattern. The LAI* is generally more homogeneously distributed within the broadleaf canopy. The mean LAI* per study plot reflects the canopy openness visible in the top-view with 2.37 m$^2$/m$^2$ in the coniferous and 14.07 m$^2$/m$^2$ in the deciduous forest. Vertically, the coniferous forest shows a bell shape with the highest mean LAI* (per 0.25 m high layer) values in the middle of the canopy (0.035 m$^2$/m$^2$), mainly due to the shape of the spruce trees and lack of understory vegetation. The deciduous forest generally has a denser canopy, with the highest values at the top of the canopy (0.15 m$^2$/m$^2$) and moderate, homogenous LAI* from the middle to bottom (0.085–0.1 m$^2$/m$^2$).

The difference in forest structure affects the distribution of APAR. The top view panels in Fig. 5 indicate a more heterogeneous APAR distribution in the coniferous forest, with several sun-facing canopy areas showing high APAR of up to 1572 W/m$^2$ (mean 126 W/m$^2$). The deciduous forest canopy shows a relatively homogenous APAR distribution with values reaching 1366 W/m$^2$ (mean 115 W/m$^2$). The middle and right panels of Fig. 5 illustrate that most APAR occurs in the top third of the deciduous canopy (19.4 W/m$^2$), with very low APAR values in the lower canopy (1.5 W/m$^2$), except for understory vegetation (3.5 W/m$^2$). The coniferous forest also shows the highest APAR in the top third of the canopy (8.1 W/m$^2$) but a steadier decrease towards the bottom of the canopy. The side view panel additionally shows high APAR in the clearing of the coniferous forest (20 W/m$^2$). These values

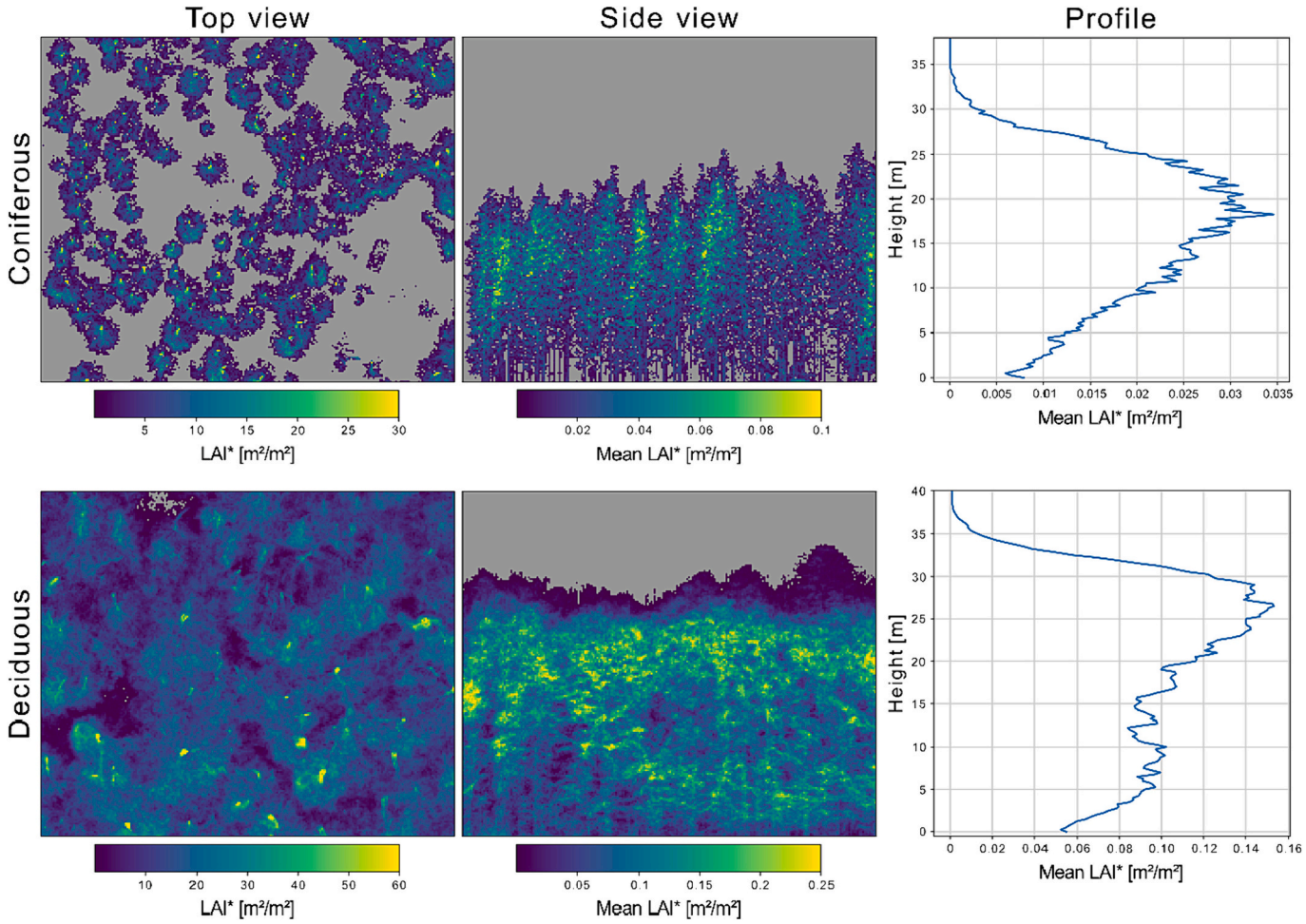


**Fig. 4.** 3D distribution of estimated leaf area index (LAI*) obtained from LiDAR measurements using AMAPVox. Left: Top view of the cumulative LAI*. North is at the top of the top view images. Middle: Side view of the mean layer LAI* in south-north direction. Right: LAI* distribution displayed as a height profile using the mean for each voxel layer (0.25 m). LAI* $< 0.01$ $m^2/m^2$ is colored grey.

are filtered out in the profile panels to simplify readability.

### 3.3. Correspondence of LAI and APAR derived from 3D and remote sensing imagery simulations

The DART simulated top-of-canopy BRF images were used to calculate RS-based APAR and LAI products for comparison with those derived from the detailed 3D data (cf. Fig. 6). The RS-based LAI in the deciduous forest shows a 9.5 $m^2/m^2$ underestimate (median absolute difference; cf. Table 3). The RS-based LAI of the coniferous forest overestimates by 0.2 $m^2/m^2$ compared to the 3D-based LAI* (Table 3). While the LAI* shows a conical distribution around single spruce trees, the RS-derived LAI seems to reflect illumination and shadow patterns instead of the 3D observed LAI dynamics. This pattern is also reflected in the spatial distribution of the relative differences. In fact, it appears that the crowns are split into two parts with high RS-based LAI values (coniferous: 2–2.5 $m^2/m^2$, deciduous: 6–7 $m^2/m^2$) on the sun-facing crown and a low LAI (coniferous: <1 $m^2/m^2$, deciduous: <2.5 $m^2/m^2$) on the shaded crown areas.

Fig. 7 illustrates the agreement between 3D and RS-based APAR estimates. We observe a general agreement between APAR derived from the 3D representation and the simulated BRF image with high APAR in the sun-facing direction and low APAR in shadows. We found a median absolute difference of 12.4 $W/m^2$ for the coniferous forest. For the deciduous forest, median values differed by as much as 210.3 $W/m^2$ (Table 3). Crown parts with a complex vertical structure and exposed to the sun show exceptionally high APAR when derived from the 3D radiative budget (coniferous: 1572 $W/m^2$, deciduous: 1366 $W/m^2$). This happens when several canopy layers receive total PAR that accumulates to very high numbers, even exceeding the incident PAR value at the top-of-canopy (coniferous: 453 $W/m^2$, deciduous: 444 $W/m^2$) (Widlowski et al., 2006). This phenomenon is clearly visible in the coniferous forest where the canopy is open, and therefore, more radiation can reach the sides of the trees.

### 3.4. Impact of shade on APAR and LAI derived from remote sensing data

The above analysis on the agreement between 3D and RS-based LAI and APAR indicates that differences largely depend on canopy shading. For both forest types, we found a strong gradient of the median absolute difference between 3D-based LAI* and RS-based LAI with a large underestimation in shaded areas in the deciduous forest (−11.3 $m^2/m^2$) to overestimates in fully illuminated areas in the coniferous forest (0.7 $m^2/m^2$) (Table 3). The agreement of APAR products across illumination

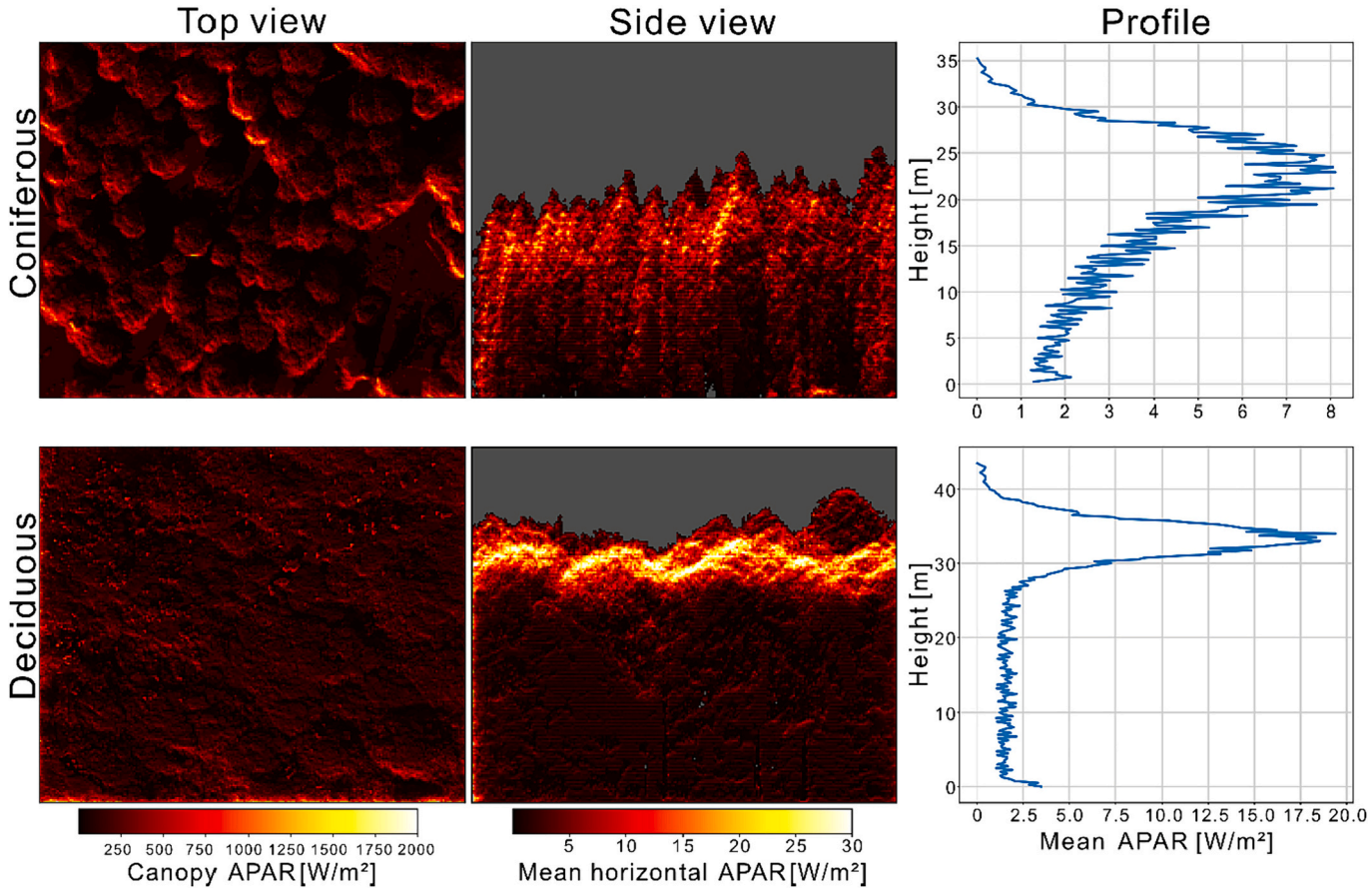


**Fig. 5.** 3D distribution of absorbed photosynthetic active radiation (APAR). Left: The top view represents the integral of the APAR for the whole vertical voxel column. Middle: The side view shows the mean layer APAR in south-north direction. Right: APAR distribution displayed as a height profile using the mean for each voxel layer (0.25 m). APAR < 0.01 $W/m^2$ is colored grey.

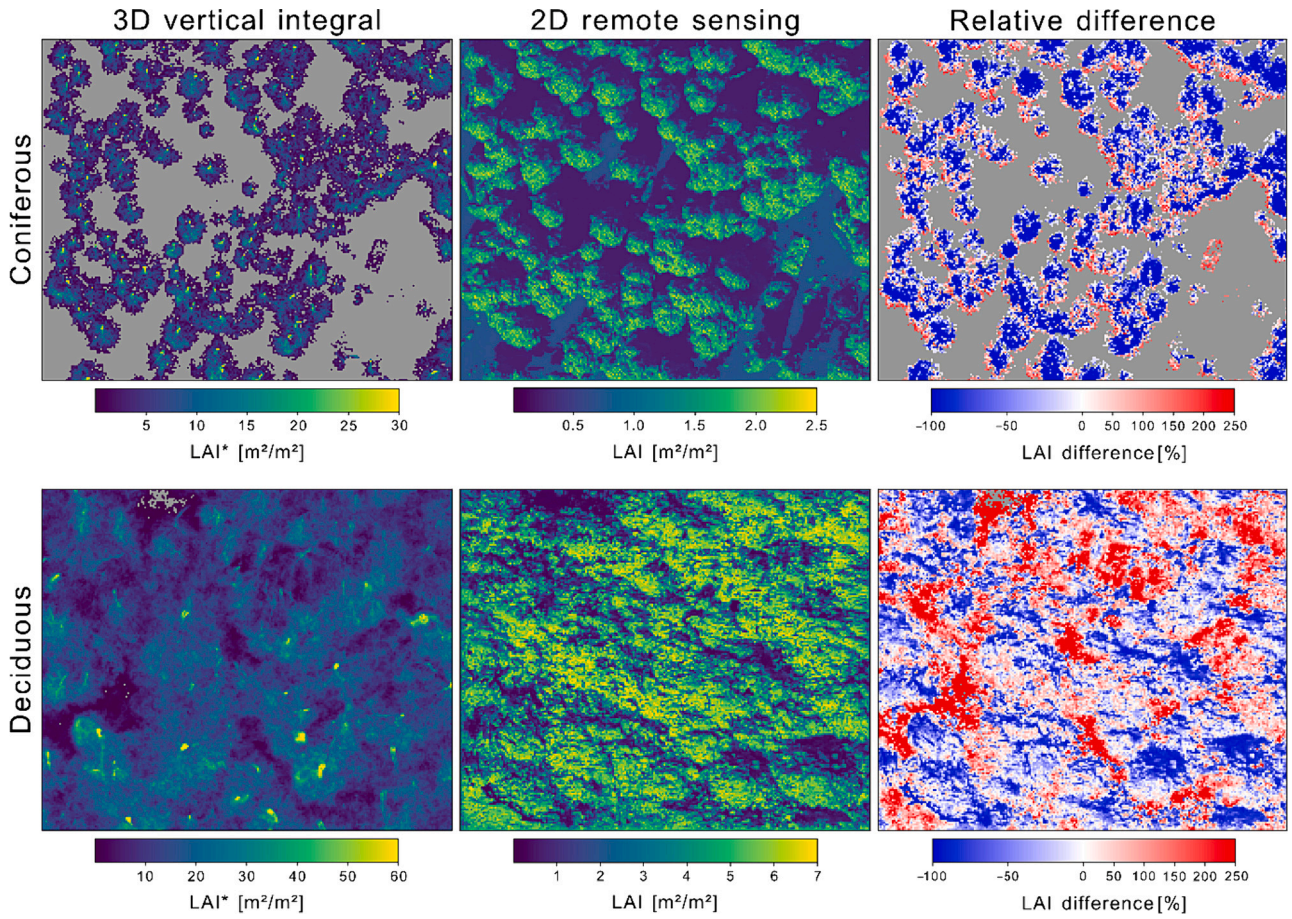


**Fig. 6.** Comparison of the estimated leaf area index (LAI*) obtained from LiDAR measurements using AMAPVox (left) and the leaf area index (LAI) derived from simulated remote sensing data (middle) for the coniferous and deciduous forest sites. The relative difference map with 2D data linearly stretched to have the same mean as the 3D data for better visibility (right) colors pixels where LAI* > LAI in blue and LAI* < LAI in red. A value of 0 indicates no relative difference between the two products. LAI or LAI* < 0.01 $m^2/m^2$ is colored grey. (For interpretation of the references to color in this figure legend, the reader is referred to the web version of this article.)

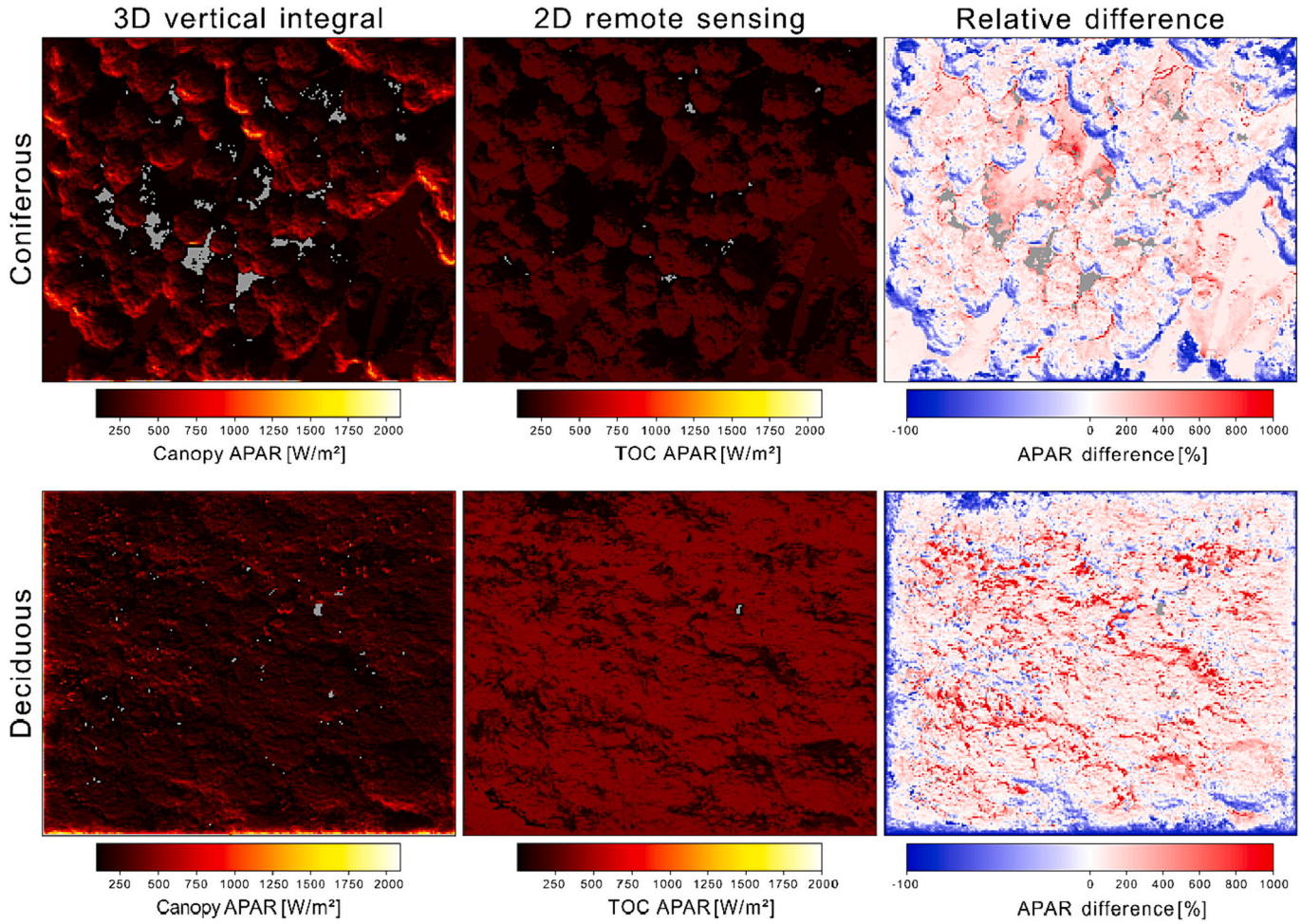


**Fig. 7.** Comparison of the absorbed photosynthetic active radiation (APAR) calculated from the 3D simulated radiative budget absorbed light per vertical voxel column (left) and using simulated remote sensing top of canopy images (middle) calculated from the modified triangular vegetation index 2 (MTVI2) and incident photosynthetic active radiation (PAR). The relative difference map with 2D data linearly stretched to have the same mean as the 3D data for better visibility (right) colors pixels where Canopy APAR > TOC APAR in blue and Canopy APAR < TOC APAR in red. A value of 0 indicates no relative difference between the two products. APAR < 1 W/m$^2$ or NaN is colored grey. (For interpretation of the references to color in this figure legend, the reader is referred to the web version of this article.)

**Table 3**
Statistics for absorbed photosynthetic active radiation (APAR), leaf area index (LAI), and estimated leaf area index (LAI*) for the top-of-canopy 2D and canopy 3D cases. Median/mean values for the whole scenes (2D and 3D) and the absolute (2D-3D) and relative ((2D-3D/3D*100%)) pixel-wise differences between the 3D LAI* and TOC 2D LAI, and 3D APAR and TOC 2D APAR.

| Parameter | Coniferous forest | | | | Deciduous forest | | | |
|---|---|---|---|---|---|---|---|---|
| | Total | Shaded | Mixed | Illum. | Total | Shaded | Mixed | Illum. |
| 3D APAR [W m$^{-2}$] | 87.7/136.7 | 6.4/16.4 | 112.9/169.0 | 190.9/257.9 | 100.7/153.4 | 97.1/114.8 | 99.2/154.5 | 109.6/210.1 |
| 2D APAR [W m$^{-2}$] | 139.9/125.4 | 13.6/15.6 | 179.2/164.3 | 251.9/218.1 | 345.4/303.5 | 345.0/304.0 | 342.8/300.7 | 350.0/308.1 |
| Abs. diff. APAR [W m$^{-2}$] | 12.4/−11.3 | 4.1/−0.8 | 42.8/−4.7 | 47.6/−39.8 | 210.3/150.1 | 84.7/189.2 | 221.7/146.2 | 229.7/98.0 |
| Rel. diff. APAR [%] | 53.6/−8.3 | 96.7/−4.9 | 55.6/−2.8 | 33.7/−15.4 | 239.0/97.8 | 878.5/164.8 | 280.1/94.6 | 136.4/46.6 |
| 3D LAI* [m$^2$ m$^{-2}$] | 1.0/2.4 | 0.0/1.1 | 2.0/3.3 | 0.0/2.5 | 13.1/14.1 | 13.1/14.1 | 13.1/14.2 | 12.9/13.9 |
| 2D LAI [m$^2$ m$^{-2}$] | 0.7/0.8 | 0.2/0.3 | 0.9/0.9 | 1.7/1.4 | 3.8/3.5 | 3.8/3.5 | 3.7/3.5 | 4.0/3.6 |
| Abs. diff. LAI [m$^2$ m$^{-2}$] | 0.2/−1.6 | 0.2/−0.8 | −1.0/−2.4 | 0.7/−1.1 | −9.5/−10.6 | −11.3/−10.6 | −9.9/−10.7 | −7.7/−10.3 |
| Rel. diff. LAI [%] | −111.0/−66.7 | −74.4/−72.7 | −112.2/−72.7 | −97.8/−44.0 | −73.5/−75.2 | −95.6/−75.2 | −75.8/−75.4 | −56.8/−74.1 |

**Table 4**
Normalized (by 3D simulation mean) relative root mean square error [%], the median relative difference [%], and the Pearson correlation coefficient for the comparison between DART simulated bi-directional reflectance and HyPlant measured hemispherical-conical reflectance factor in nine different bands.

| Simulated band [nm] | Coniferous forest | | | Deciduous forest | | |
|---|---|---|---|---|---|---|
| | nRMSE [%] | Rel. diff. [%] | Pearson's R | nRMSE [%] | Rel. diff. [%] | Pearson's R |
| 528–532 | 71.2 | −21.9 | 0.47 | 59.8 | −30.8 | 0.09 |
| 547–554 | 74.8 | −25.7 | 0.48 | 79.5 | −39.5 | 0.1 |
| 569–573 | 82.2 | −32.5 | 0.51 | 89.7 | −42.8 | 0.09 |
| 644–679 | 109 | −44.9 | 0.59 | 61.4 | −29.8 | 0.05 |
| 667–674 | 109.8 | −45.2 | 0.59 | 63.2 | −30.4 | 0.05 |
| 795–810 | 64.7 | −19.3 | 0.35 | 30.8 | 5.6 | 0.16 |
| 797–804 | 64.5 | −19.2 | 0.35 | 30.8 | 5.8 | 0.16 |
| 890–905 | 67.7 | −22.8 | 0.36 | 32.1 | 19.6 | 0.16 |
| 955–970 | 70.3 | 11.3 | 0.36 | 31.0 | 0.2 | 0.16 |

conditions differs largely as well. For both forest types, APAR was overestimated in all illumination classes of the RS product, with an increasing overestimation with increasing illumination (up to 229.7 W/m$^2$ in the illuminated deciduous class) (Table 3).

### 3.5. Comparison of simulated vs. measured airborne imagery

We compared the DART simulated BRF data (cf. Section 2.3.2) against measured HyPlant HCRF data to investigate the general agreement of both and judge the impact of applied simplifications during the simulation. Table 4 illustrates that the differences vary depending on the wavelength and study site. The BRF overestimates as much as 19.6% and underestimates up to 45.2%. The observed differences can be related to the physical units represented in the BRF and HCRF images and simplifications applied during the simulation (cf. Figs. A2, A3 in the Appendix for map representation).

The 3D-based BRF values are strongly underestimated in the visible wavelengths across both study sites, which is reflected in the negative median relative difference values (coniferous: −45.2% to −21.9%, deciduous: −42.8% to −30.4%) and high nRMSE values (coniferous: 71.2% to 109.8%, deciduous: 59.8% to 89.7%). The difference between the two products is much smaller in the NIR part of the spectrum. In the coniferous forest, an underestimation is still present, except for the 955–970 nm band, which shows an overestimation of 11.3% in the simulated 3D product (Table 4). The NIR bands for the deciduous forest all overestimated the 3D-based BRF data, with the 955–970 nm band performing the best with a 0.2% median relative difference. The underlying Pearson's correlation coefficients per spectral band are very low in the deciduous site (Pearson's $R$ = 0.05–0.16) and moderate in the coniferous site (Pearson's $R$ = 0.35–0.59) (Table 4; cf. Figs. A2–A5 in the Appendix for visual representation).

## 4. Discussion

### 4.1. Dynamics of LAI and APAR derived from simulations and remote sensing

We observed contrasting 3D forest structures represented here via the LAI*. Tree crowns in the deciduous forest are much denser at the top and overlap, resulting in a more homogeneous LAI* distribution from a top view perspective. In contrast, the LAI* distribution in the coniferous forest with more considerable distances between individual trees is more heterogeneous. This corresponds well with the results of multiple studies (Hagemeier and Leuschner, 2019; Lalic et al., 2013; Lalic and Mihailovic, 2004). At the individual tree scale, LAI* in the coniferous crowns is also known to be influenced by needle clumping and, thus, occlusion within the top of the crowns (Schraik et al., 2021, 2023). Béland and Kobayashi (2024) showed that clumping is one of the main drivers for the canopy reflectance, especially in the NIR wavelength range. The structural variation also largely influences the retrieval of APAR information (Lin et al., 2018). We observe the highest absorption in the deciduous forest directly above the densest canopy part. The lower density in the coniferous forest with its triangular-shaped crowns allows the light to reach deeper canopy layers, resulting in an increased vertical distribution of APAR (Guillevic and Gastellu-Etchegorry, 1999; Kükenbrink et al., 2021). Results indicate that simplified assumptions on the vertical distribution of LAI and APAR can cause uncertainties in related RS-based estimates and subsequently derived gas exchange products (Damm et al., 2020; Firanj et al., 2015; Kükenbrink et al., 2019).

The comparison of both forest types reveals substantial differences in LAI and APAR in 3D but also in the simulated RS BRF images representing the outer canopy layer. This difference can be related to a limited vertical sensitivity of RS. Particularly the contrasting spatial patterns of LAI and APAR derived from 3D simulations and RS imply that the parameters calculated from RS data depend not only on the structure of the forests, as shown in Zeng et al. (2023), but also on other effects. In fact, several studies indicate that inherent assumptions during the retrieval of surface reflectance (i.e., the assumption that the composition of diffuse and direct irradiance is relatively constant over the entire canopy) can cause large artifacts in retrieved RS products (Damm et al., 2015; Fawcett et al., 2018; Kükenbrink et al., 2019). This can be explained by the sometimes large difference between the assumption of a relatively homogenous top-of-canopy irradiance (note the dependence of diffuse irradiance on surface reflectance) and the effective irradiance at the surface level (i.e., a leaf or tree crown). This difference is wavelength-dependent and changes with observation and illumination angle, atmospheric state, and tree geometry (via cast shadows of trees on neighboring trees, shadowing of individual tree crowns, and multiple scattering between neighboring trees). Particularly, the wavelength dependency causes large artifacts in retrieved RS products and problems in interpreting insufficiently corrected data (Damm et al., 2015; Fawcett et al., 2018; Kükenbrink et al., 2019). Our findings confirm that such assumptions during atmospheric correction procedures can lead to considerable differences between the top-of-canopy RS products and their 3D representations.

### 4.2. Agreement of simulated BRF and measured HCRF values

The observed patterns in the simulated BRF and the acquired HCRF data of the coniferous forest agree, considering the many assumptions made during the simulation process (i.e., constant leaf optical properties, LIDF). In addition, BRF and HCRF represent different physical units. While BRF considers directional irradiance only along the direct path of sunrays, HCRF considers hemispheric irradiance with particularly the diffuse irradiance component from the entire hemisphere (cf. Schaepman-Strub et al. (2006) or Schunke et al. (2023) for more details about BRF and HCRF differences). Pixels representing sunlit canopy areas show the highest agreement between BRF simulation and HCRF measurement at both sites, mainly since the assumption of full illumination is least violated in such areas. This finding agrees with another study by Janoutová et al. (2019), where an overestimation of simulated reflectance in the visible region of the spectrum was found, possibly

accountable to the accuracy of the LOP and the atmospheric compensation applied in the simulation (Morsdorf et al., 2020). In contrast, Schneider et al. (2014) found an underestimation in the NIR region when simulating airborne imagery, primarily due to an insufficient structural representation of the forest (Morsdorf et al., 2020).

For shaded areas, we found a general underestimation of simulated BRF in almost all spectral bands compared to the measured HCRF values (Table 4), which was expected. The theoretical difference between BRF and HCRF can again explain this divergence. In the DART simulated BRF values, the considered amount of diffuse irradiance is lower compared to the measurement case (HCRF), as only diffuse irradiance along the direct sun rays is considered, and the diffuse irradiance from the remaining hemisphere is missing. One can interpret the BRF as an extreme case of HCRF for very clear sky conditions with no aerosols; in fact, observed BRF values close to 0% indicate a substantially reduced amount of scattered light due to hemispheric irradiance and multiple scattering. A recent study quantified the effect and reported more than 10% differences between BRF and HCRF for larger view zenith angles and aerosol-rich atmospheres (Schunke et al., 2023). Still, another contribution could be an overestimation of LAD. If the canopy density is too high, light scattered through leaf gaps or transmitted light is small, resulting in a low irradiance and reflected radiance. Thus, calculated BRF is error-prone when assuming a constant irradiance over the entire scene. Consequently, the BRF simulation underestimates the reflectance, and APAR and LAI derived from this data contrast more between shaded and illuminated canopy areas.

Concerning the processing of the used HyPlant airborne imaging spectroscopy data: The data were corrected for topographic effects (modified Minnaerd method) and nadir adjusted in ATCOR-4 to obtain HCRF values. In this process, the atmosphere and related irradiance are approximated with a set of best-guessed parameters (e.g., aerosol model, vertical stratification), image-derived parameters (e.g., aerosol load, water vapor content), and auxiliary topography information via digital elevation models. The applied assumptions possibly yield uncertainties in the retrieved HCRF image, but the even larger effect is the above-mentioned assumption of almost constant irradiance over the entire scene (except for irradiance variations accounted for by the standard processing). The advancement of atmospheric correction schemes that consider the effective irradiance at the canopy level could open new possibilities to compensate for this illumination problem. Ideas in this direction were already presented, for example, the use of p-theory based approaches (as demonstrated for VNIR in Ihalainen et al. (2023)) to accurately estimate irradiance at the pixel level. The use of additional data such as 3D object models is interesting, while several complications (e.g., lack of detailed 3D object models, geometric misalignment of optical and 3D data for elevated objects with increasing distance from nadir, the inability of atmospheric correction tools to simulate multiple scattering due to neighboring trees, etc.) were reported in Fawcett et al. (2018) making such a correction practically impossible. A yet different approach is shifting the retrieval of RS products from top-of-canopy to top-of-atmosphere using coupled atmosphere and surface radiative transfer models. The combination of these models theoretically allows the retrieval of the actual composition of diffuse and direct irradiance together with vegetation information and even improves the representation of the sequence of light interactions with the atmosphere and the canopy. Laurent et al. (2011a, 2011b, 2013) already tested this approach with promising results.

### 4.3. Limitations of our approach and possible ways forward

#### 4.3.1. Data acquisition

One limitation of our study lies in the sub-optimal data acquisition for both sites since LOP, LiDAR, and airborne data could not be acquired simultaneously. The LiDAR and HyPlant data were collected the same week in June 2021 at the coniferous forest site, whereas the LOP were measured in September. The differences in simulated BRF and measured HCRF could partly originate from this fact since the leaf or needle optical properties vary during the year (Lukeš et al., 2020; Morsdorf et al., 2009). At the deciduous site, the time between LiDAR and optical airborne data acquisition is up to seven years. This time difference implies that the structural information used for the simulation could be outdated in the sense that trees might not exist anymore or have changed height and shape. This discontinuity may be one of the reasons that the correlation between simulated BRF and airborne-based HCRF is much lower in this study site. The last in situ measured LOP date back to 2009, so we opted for database spectra for this site. Using data acquired at the same time of year is recommended for such simulations. In addition, a sensitivity analysis on the effect of temporal dynamics in the LOP and canopy structure on the simulated BRF would be helpful to quantify the implications of the presented results. Additionally, using different LiDAR sensor setups in both sites can also lead to uncertainties in the result. Using a voxel-based approach, we partly compensate for the distribution of different point cloud densities, potentially reducing the impact of combining different LiDAR sensors. We recommend using the same sensor and survey configurations whenever possible for future studies.

#### 4.3.2. Challenges in creating 3D virtual forest scenes for radiative transfer simulations

Another limitation of our approach is using various assumptions and simplifications to generate the 3D virtual scene and the possible uncertainties introduced. Separating the point cloud into wood and foliage was particularly challenging (Wang et al., 2020). Although the method used in our study worked well, it only recognized big tree trunks as wood, while smaller branches were classified as leaves or needles. This may have overestimated the retrieved vegetation density and mixed voxels, especially in the tree crowns, influencing the simulated canopy reflectance. Malenovský et al. (2008) found that canopy reflectance can increase up to 2% in the red part of the spectrum in the presence of mixed pixels, while this overestimation can affect the calculation of additional parameters using indices like the normalized difference vegetation index (NDVI) (Leblanc et al., 1997). Reconstructing the woody surface from the separated point clouds worked better in the coniferous forest, mainly because the Norway spruce trunks are mostly straight compared to the curved trunks of deciduous trees. The Poisson surface reconstruction showed limitations in reconstructing branching trees, mainly due to the need for more data points in the denser canopy (Eysn et al., 2013). Quantitative structure models could be used to reconstruct the woody elements from classified point clouds (Lau et al., 2018). However, analyzing a whole forest canopy instead of single tree point clouds makes this process more complex and time-consuming (Disney et al., 2018).

The canopy structure and related LAD dynamics substantially impact the simulated reflectance images as the 3D distribution of this parameter largely determines the crown topography and, thus, the geometric optical scattering (Ollinger, 2011). Further, quantifying the LAD using the AMAPVox software is subject to uncertainty as an assumption about the LIDF, describing the volumetric scattering, must be made to track those

laser beams that drive the voxel density. Due to the large complexity of natural forests and the lack of spatial LIDF information, it is challenging to reproduce forest sites 1:1. Consequently, we decided to use only one LIDF value from previous studies for the entire study plot per forest even if the LIDF is known to largely differ within the forest and even within a tree (Liu et al., 2019).

The virtual scenes were normalized for topography to allow better comparability between the two forest sites, as they have very different slopes (Kükenbrink et al., 2021). This process, however, causes differences in the simulated illumination pattern within the crowns compared to its airborne measured counterpart, which images the real world with topography. Further, edge effects in the direction of the sun are prominent as the trees outside the simulated plot are excluded and, therefore, do not shade trees and surfaces in the DART scene. Increasing the area of the TLS acquisition by a buffer zone would be a strategy to compensate for this problem.

However, the created virtual scenes and simulations are consistent in that they share the same underlying assumptions. This allows us to address the key aspect of our paper: demonstrating that RS and 3D products largely differ due to geometric optical scattering and the limited vertical sensitivity of optical RS data.

#### 4.3.3. Forest site selection

Lastly, we only evaluated two specific forest ecosystem sites in Switzerland, which limits the representativity of our findings. Including more vegetation types in such an analysis would be essential in generalizing our findings on the influence of forest structure on RS estimates of HCRF and derived LAI and APAR.

## 5. Conclusions

Our findings demonstrate a complex divergence between RS reflectance-based estimates of LAI and APAR compared to their modeled 3D variation in complex structured forest canopies. We conclude that the diverging pattern can be attributed to i) an insensitivity of optical RS measurements for the vertical distribution of LAI and APAR and ii) assumptions about irradiance dynamics over heterogeneous forest canopies made during the process of reflectance retrievals. The latter effect was found to dominate the disagreement between 3D and RS-derived information. We recommend future research to explore the limitations and options of optical RS in capturing the 3D dynamics of forest information, such as LAI and APAR. This includes i) a thorough examination of the wavelength-dependent light interaction with the canopy, ii) the advancement of analytical strategies to account for shadowing effects and vertical insensitivity, and iii) the exploration of scale dependencies of shadowing across spatial resolution provided by RS systems. We suggest considering insights derived from our study for the interpretation of RS products and for the advancement of approaches that build upon such RS-derived information for estimates of higher-level products like gas exchange estimates.

## Funding

We acknowledge funding by the Swiss National Science Foundation (SNSF) project Fluo4Eco (grant number 197243).

## CRediT authorship contribution statement

**Jasmin Kesselring:** Writing – review & editing, Writing – original draft, Formal analysis, Data curation, Conceptualization. **Felix Morsdorf:** Writing – review & editing, Writing – original draft, Resources, Methodology. **Daniel Kükenbrink:** Writing – review & editing, Writing – original draft, Methodology, Data curation. **Jean-Philippe Gastellu-Etchegorry:** Software. **Alexander Damm:** Writing – review & editing, Writing – original draft, Project administration, Funding acquisition, Conceptualization.

## Declaration of competing interest

The authors declare no conflict of interest.

## Data availability

Data will be made available on request.

## Acknowledgments

We thank Veronika Oehl and Joan Sturm for their support in acquiring TLS and leaf optical properties measurements. We also thank Jennifer Adams for the fruitful discussions and the four anonymous reviewers for their helpful comments. Last, we thank the HyPlant team, particularly Uwe Rascher and Patrick Rademske from the Forschungszentrum Jülich, for processing the HyPlant data and hosting this airborne research infrastructure.

## Appendix

**Table A1**
Parameter settings used for the RANSAC shape detection algorithm in CloudCompare.

| Parameter | Coniferous forest | Deciduous forest |
|---|---|---|
| Max. distance to primitive | 0.15 | 0.169 |
| Sampling resolution | 0.3 | 0.336 |
| Max. normal deviation | 10° | 25 |
| Overlooking probability | 0.01 | 0.01 |

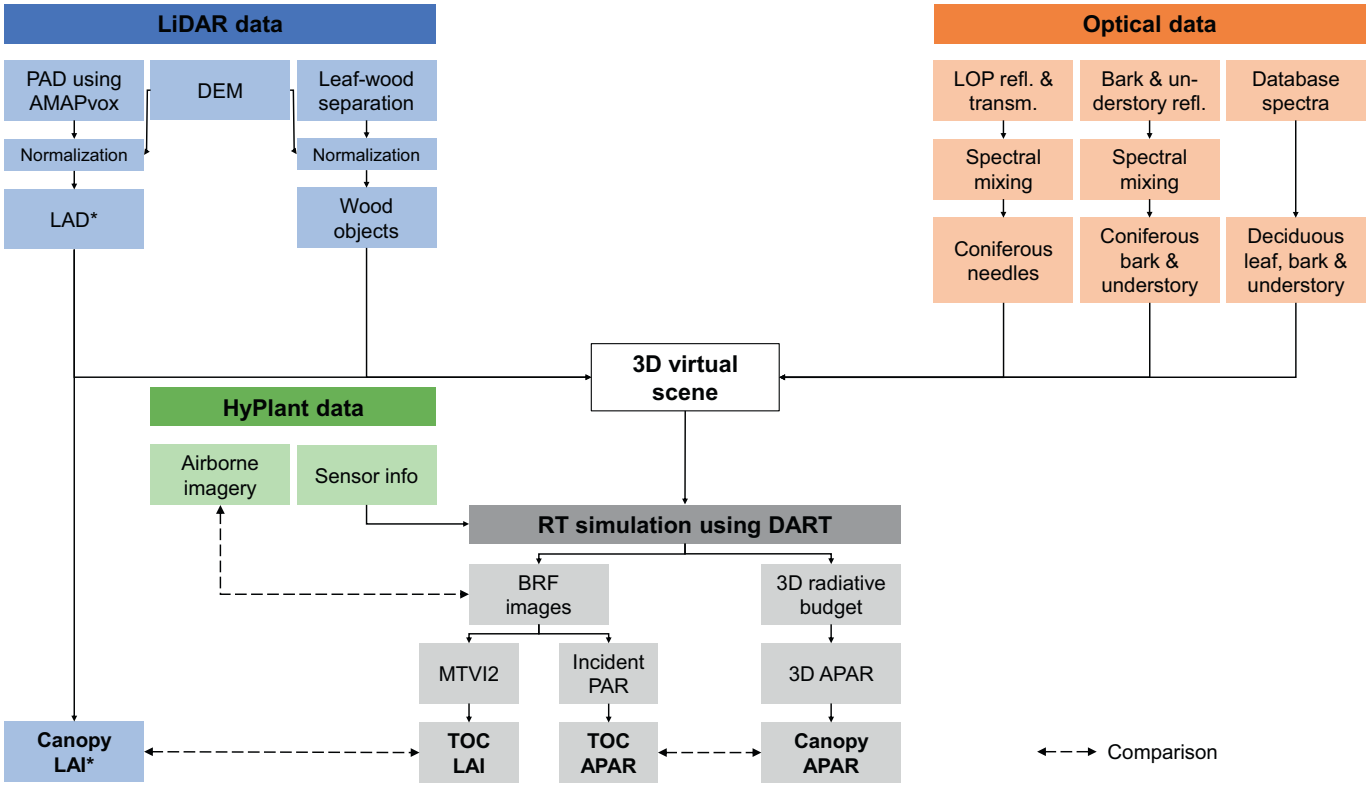


**Fig. A1.** Overview of data, methods, and products. LiDAR-derived data in blue, optical data in orange, airborne imagery in green and all products derived from the DART simulation in grey. The comparison between two products is depicted as a dashed arrow. (For interpretation of the references to color in this figure legend, the reader is referred to the web version of this article.)

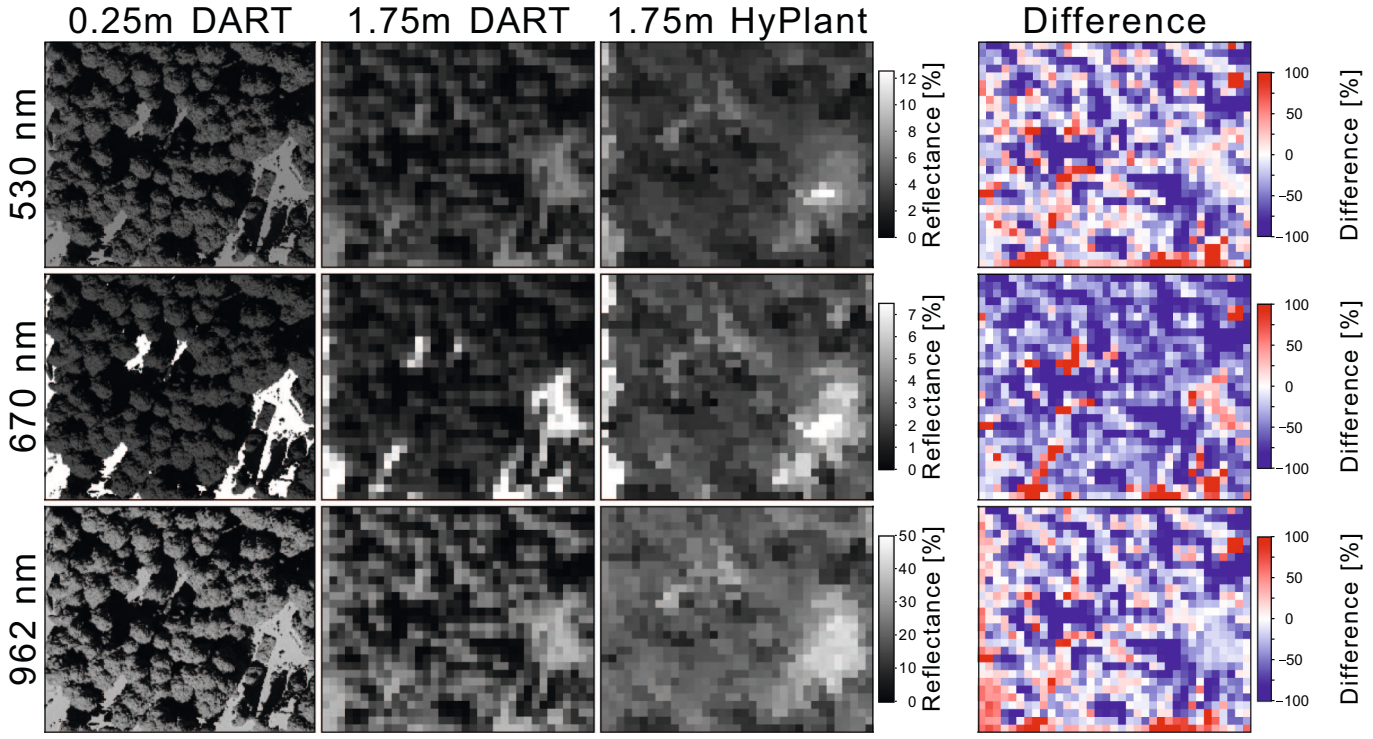


**Fig. A2.** Coniferous site: simulated top of canopy bi-directional reflectance (BRF) images of three bands (530 nm, 670 nm, 962 nm) and HyPlant hemispherical-conical reflectance factors (HCRF) at their corresponding bands. Columns from left to right: original resolution of the DART simulation (0.25 m), DART output convolved to the HyPlant sensor resolution (1.75 m) using a 9 × 9 kernel and a weighted average, original HyPlant image clipped to the study site, and the relative difference between real HyPlant and the simulated top of canopy reflectance. A value of 0 indicates no difference between the two products, red colors indicate a higher reflectance value in the DART simulation than in the HyPlant pixel, and blue lower values in the simulated product than in the actual image. (For interpretation of the references to color in this figure legend, the reader is referred to the web version of this article.)

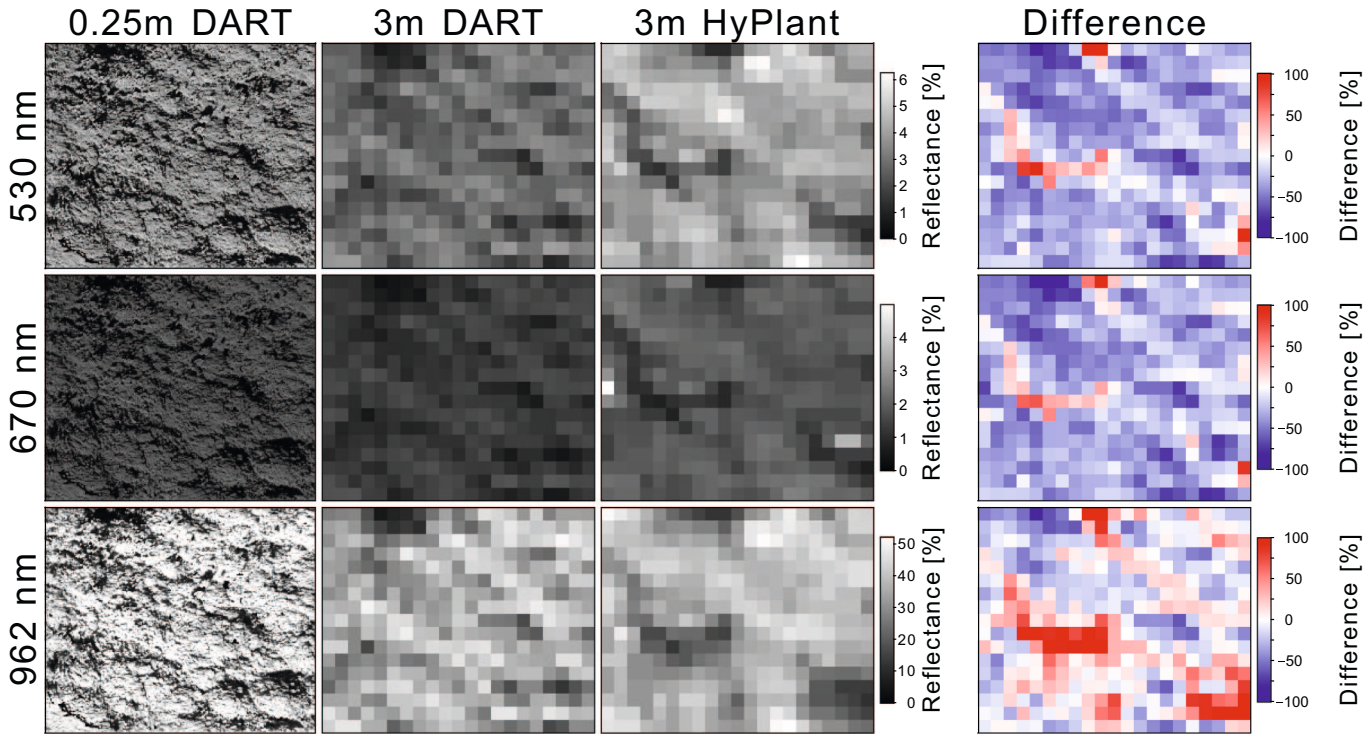


**Fig. A3.** Deciduous site: simulated top of canopy bi-directional reflectance (BRF) images of three bands (530 nm, 670 nm, 962 nm) and HyPlant hemispherical-conical reflectance factors (HCRF) at their corresponding bands. Columns from left to right: original resolution of the DART simulation (0.25 m), DART output convolved to the HyPlant sensor resolution (3 m) using a 15 × 15 kernel and a weighted average, original HyPlant image clipped to the study site, and the relative difference between real HyPlant and the simulated top of canopy reflectance. A value of 0 indicates no difference between the two products, red colors indicate a higher reflectance value in the DART simulation than in the HyPlant pixel, and blue lower values in the simulated product than in the actual image. (For interpretation of the references to color in this figure legend, the reader is referred to the web version of this article.)

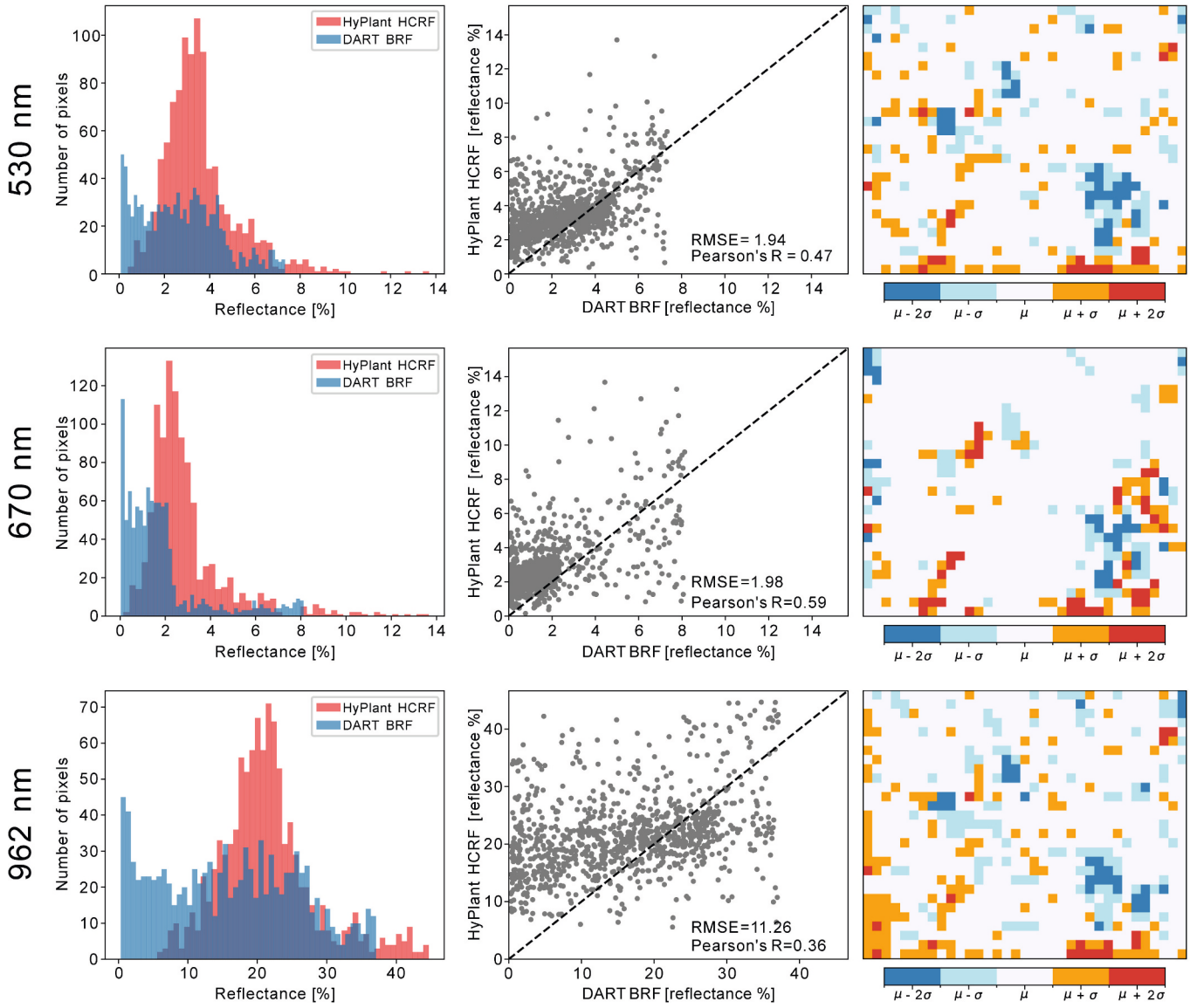


**Fig. A4.** Coniferous site: comparison of the DART simulated bi-directional reflectance (BRF) and HyPlant measured hemispheric-conical reflectance factor (HCRF) values of three bands (530 nm, 670 nm, 962 nm). Columns from left to right: histogram of BRF (blue) and HCRF (red) values. Scatterplot of DART-based BRF data on the x-axis and HyPlant-based HCRF values on the y-axis, the 1:1 line is superimposed as a dotted line, Pearson's R stands for the Pearson correlation coefficient, and the RMSE for the root mean standard error of the two data sets. Difference image between simulated top-of-canopy BRF and measured HCRF reflectance classified according to their mean and standard deviation. (For interpretation of the references to color in this figure legend, the reader is referred to the web version of this article.)

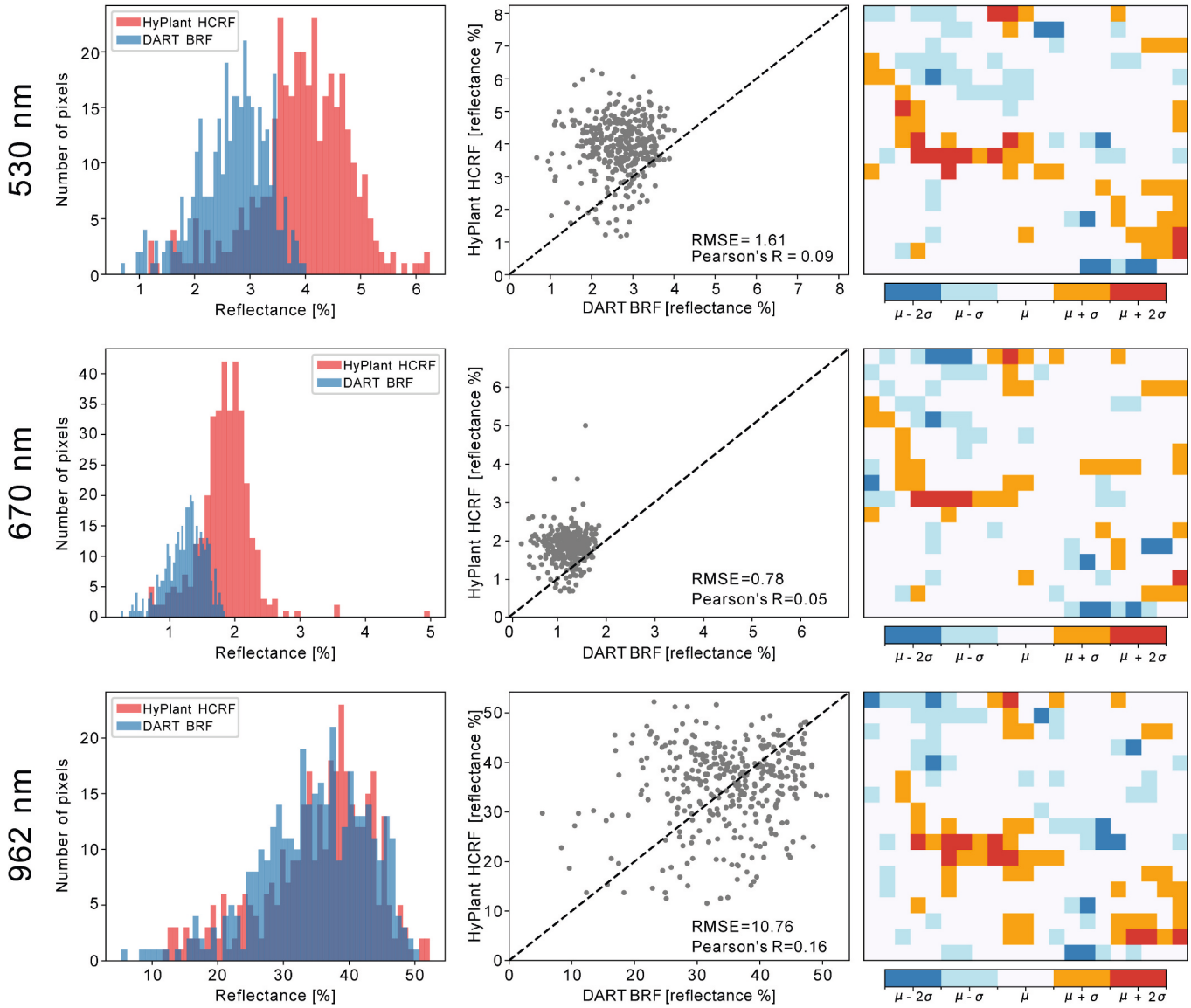


**Fig. A5.** Deciduous site: comparison of the DART simulated bi-directional reflectance (BRF) and HyPlant measured hemispheric-conical reflectance factor (HCRF) values of three bands (530 nm, 670 nm, 962 nm). Columns from left to right: histogram of BRF (blue) and HCRF (red) values. Scatterplot of DART-based BRF data on the x-axis and HyPlant-based HCRF values on the y-axis, the 1:1 line is superimposed as a dotted line, Pearson's R stands for the Pearson correlation coefficient, and the RMSE for the root mean standard error of the two data sets. Difference image between simulated top-of-canopy BRF and measured HCRF reflectance classified according to their mean and standard deviation. (For interpretation of the references to color in this figure legend, the reader is referred to the web version of this article.)

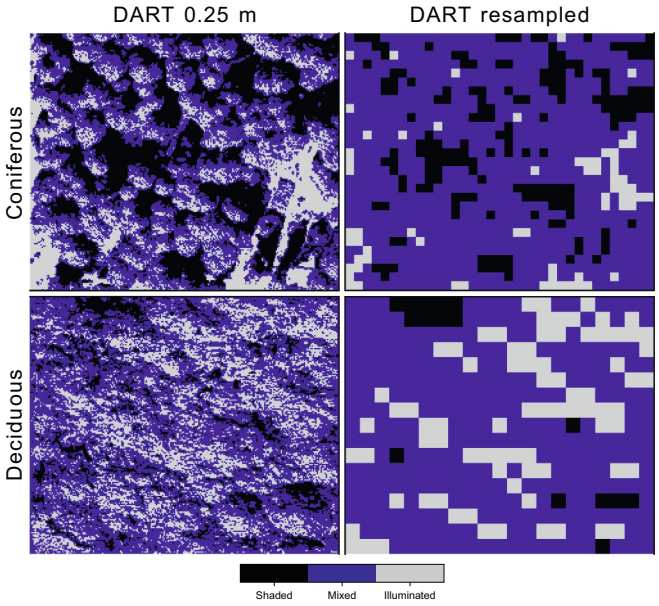


**Fig. A6.** NIR band (795–810 nm) classified into shaded, mixed, and illuminated pixels in both the coniferous and deciduous forests. Left: original DART resolution BRF image (0.25 m) classified with reflectance < 4% as shaded pixels and > 29.5% as illuminated pixels in the coniferous case and reflectance < 15% as shaded pixels and > 52% as illuminated pixels in the deciduous case. Right: convolved to HyPlant resolution DART BRF image (coniferous: 1.75 m, deciduous: 3 m) classified with reflectance < 5% as shaded pixels and > 29.5% as illuminated pixels in the coniferous case and reflectance < 20% as shaded pixels and > 45% as illuminated pixels in the deciduous case.

## References


Anderson, M.C., Allen, R.G., Morse, A., Kustas, W.P., 2012. Use of Landsat thermal imagery in monitoring evapotranspiration and managing water resources. Remote Sens. Environ. 122, 50–65. https://doi.org/10.1016/j.rse.2011.08.025.

Baldocchi, D., 2003. Assessing the eddy covariance technique for evaluating carbon dioxide exchange rates of ecosystems: past, present and future. Glob. Chang. Biol. 9, 479–492. https://doi.org/10.1046/j.1365-2486.2003.00629.x.

Baldocchi, D., Falge, E., Gu, L., Olson, R., Hollinger, D., Running, S., Anthoni, P., Bernhofer, C., Davis, K., Evans, R., Fuentes, J., Goldstein, A., Katul, G., Law, B., Lee, X., Malhi, Y., Meyers, T., Munger, W., Oechel, W., Paw, K.T., Pilegaard, K., Schmid, H.P., Valentini, R., Verma, S., Vesala, T., Wilson, K., Wofsy, S., 2001. FLUXNET: a new tool to study the temporal and spatial variability of ecosystem–scale carbon dioxide, water vapor, and energy flux densities. Bull. Am. Meteorol. Soc. 82, 2415–2434. https://doi.org/10.1175/1520-0477(2001)082<2415:FANTTS>2.3.CO;2.

Baldocchi, D.D., Wilson, K.B., Gu, L., 2002. How the Environment, Canopy Structure and Canopy Physiological Functioning Influence Carbon, Water and Energy Fluxes of a Temperate Broad-Leaved Deciduous Forest - an Assessment with the Biophysical Model CANOAK. Oxford Academic, pp. 1065–1077. https://doi.org/10.1093/treephys/22.15-16.1065.

Béland, M., Kobayashi, H., 2024. Drivers of deciduous forest near-infrared reflectance: a 3D radiative transfer modeling exercise based on ground lidar. Remote Sens. Environ. 302, 113951 https://doi.org/10.1016/j.rse.2023.113951.

Bonan, G.B., Patton, E.G., Finnigan, J.J., Baldocchi, D.D., Harman, I.N., 2021. Moving beyond the incorrect but useful paradigm: reevaluating big-leaf and multilayer plant canopies to model biosphere-atmosphere fluxes – a review. Agric. For. Meteorol. 306, 108435 https://doi.org/10.1016/j.agrformet.2021.108435.

Braun, D., Damm, A., Paul-Limoges, E., Revill, A., Buchmann, N., Petchey, O.L., Hein, L., Schaepman, M.E., 2017. From instantaneous to continuous: using imaging spectroscopy and in situ data to map two productivity-related ecosystem services. Ecol. Indic. 82, 409–419. https://doi.org/10.1016/j.ecolind.2017.06.045.

Burchard-Levine, V., Nieto, H., Riaño, D., Migliavacca, M., El-Madany, T.S., Guzinski, R., Carrara, A., Martín, M.P., 2021. The effect of pixel heterogeneity for remote sensing based retrievals of evapotranspiration in a semi-arid tree-grass ecosystem. Remote Sens. Environ. 260, 112440 https://doi.org/10.1016/j.rse.2021.112440.

Chen, S., Liu, L., Sui, L., Liu, X., 2022. Improving GPP estimates by partitioning green APAR from total APAR in two deciduous forest sites. J. For. Res. 1–13. https://doi.org/10.1007/s11676-022-01546-6.

Damm, A., Guanter, L., Verhoef, W., Schläpfer, D., Garbari, S., Schaepman, M.E., 2015. Impact of varying irradiance on vegetation indices and chlorophyll fluorescence derived from spectroscopy data. Remote Sens. Environ. 156, 202–215. https://doi.org/10.1016/j.rse.2014.09.031.

Damm, A., Paul-Limoges, E., Kükenbrink, D., Bachofen, C., Morsdorf, F., 2020. Remote sensing of forest gas exchange: considerations derived from a tomographic perspective. Glob. Chang. Biol. 26, 2717–2727. https://doi.org/10.1111/gcb.15007.

de Boissieu, F., Heuschmidt, F., Lauret, N., Ebengo, D.M., Vincent, G., Fret, J.-B., Yin, T., Gastellu-Etchegorry, J.-P., Costeraste, J., Lefvre-Fonollosa, M.-J., Durrieu, S., 2023. Validation of the DART model for airborne laser scanner simulations on complex forest environments. IEEE J. Sel. Top. Appl. Earth Obs. Remote Sens. 16, 8379–8394. https://doi.org/10.1109/jstars.2023.3302030.

de Conto, T., Olofsson, K., Görgens, E.B., Rodriguez, L.C.E., Almeida, G., 2017. Performance of stem denoising and stem modelling algorithms on single tree point clouds from terrestrial laser scanning. Comput. Electron. Agric. 143, 165–176. https://doi.org/10.1016/j.compag.2017.10.019.

Disney, M.I., Vicari, M.B., Burt, A., Calders, K., Lewis, S.L., Raumonen, P., Wilkes, P., 2018. Weighing trees with lasers: advances, challenges and opportunities. Interface Focus 8, 20170048. https://doi.org/10.1098/rsfs.2017.0048.

Elsherif, A., Gaulton, R., Shenkin, A., Malhi, Y., Mills, J., 2019. Three dimensional mapping of forest canopy equivalent water thickness using dual-wavelength terrestrial laser scanning. Agric. For. Meteorol. 276–277, 107627 https://doi.org/10.1016/j.agrformet.2019.107627.

Etzold, S., Ruehr, N.K., Zweifel, R., Dobbertin, M., Zingg, A., Pluess, P., Häsler, R., Eugster, W., Buchmann, N., 2011. The carbon balance of two contrasting mountain forest ecosystems in Switzerland: similar annual trends, but seasonal differences. Ecosystems 14, 1289–1309. https://doi.org/10.1007/s10021-011-9481-3.

Eysn, L., Pfeifer, N., Ressl, C., Hollaus, M., Grafl, A., Morsdorf, F., 2013. A practical approach for extracting tree models in forest environments based on equirectangular projections of terrestrial laser scans. Remote Sens. 5, 5424–5448. https://doi.org/10.3390/rs5115424.

Fawcett, D., Verhoef, W., Schläpfer, D., Schneider, F.D., Schaepman, M.E., Damm, A., 2018. Advancing retrievals of surface reflectance and vegetation indices over forest ecosystems by combining imaging spectroscopy, digital object models, and 3D canopy modelling. Remote Sens. Environ. 204, 583–595. https://doi.org/10.1016/j.rse.2017.09.040.

Firanj, A., Lalic, B., Podrascanin, Z., 2015. The impact of forest architecture parameterization on GPP simulations. Theor. Appl. Climatol. 121, 529–544. https://doi.org/10.1007/s00704-014-1251-7.

Fisher, J.B., Melton, F., Middleton, E., Hain, C., Anderson, M., Allen, R., McCabe, M.F., Hook, S., Baldocchi, D., Townsend, P.A., Kilic, A., Tu, K., Miralles, D.D., Perret, J., Lagouarde, J.P., Waliser, D., Purdy, A.J., French, A., Schimel, D., Famiglietti, J.S., Stephens, G., Wood, E.F., 2017. The future of evapotranspiration: global requirements for ecosystem functioning, carbon and climate feedbacks, agricultural management, and water resources. Water Resour. Res. 53, 2618–2626. https://doi.org/10.1002/2016wr020175.

Gastellu-Etchegorry, J.P., Yin, T., Lauret, N., Cajgfinger, T., Gregoire, T., Grau, E., Feret, J.B., Lopes, M., Guilleux, J., Dedieu, G., Malenovskỳ, Z., Cook, B.D., Morton, D., Rubio, J., Durrieu, S., Cazanave, G., Martin, E., Ristorcelli, T., 2015. Discrete anisotropic radiative transfer (DART 5) for modeling airborne and satellite spectroradiometer and LIDAR acquisitions of natural and urban landscapes. Remote Sens. 7, 1667–1701. https://doi.org/10.3390/rs70201667.

Grzesiak, M.T., Filek, W., Hura, T., Kocurek, M., Pilarski, J., 2010. Leaf optical properties during and after drought stress in triticale and maize genotypes differing in drought

tolerance. Acta Physiol. Plant. 32, 433–442. https://doi.org/10.1007/s11738-009-0400-6.
Guillevic, P., Gastellu-Etchegorry, J.P., 1999. Modeling BRF and radiation regime of boreal and tropical forest II. PAR regime. Remote Sens. Environ. 68, 317–340. https://doi.org/10.1016/s0034-4257(98)00120-5.
Haboudane, D., Miller, J.R., Pattey, E., Zarco-Tejada, P.J., Strachan, I.B., 2004. Hyperspectral vegetation indices and novel algorithms for predicting green LAI of crop canopies: modeling and validation in the context of precision agriculture. Remote Sens. Environ. 90, 337–352. https://doi.org/10.1016/j.rse.2003.12.013.
Hackel, T., Wegner, J.D., Schindler, K., 2016. Contour Detection in Unstructured 3D Point Clouds, pp. 1610–1618. https://doi.org/10.1109/cvpr.2016.178.
Hagemeier, M., Leuschner, C., 2019. Functional crown architecture of five temperate broadleaf tree species: vertical gradients in leaf morphology, leaf angle, and leaf area density. Forests 10, 265. https://doi.org/10.3390/f10030265.
Hatfield, J.L., Dold, C., 2019. Water-use efficiency: advances and challenges in a changing climate. Front. Plant Sci. 10, 103. https://doi.org/10.3389/fpls.2019.00103.
Ihalainen, O., Juola, J., Mõttus, M., 2023. Physically based illumination correction for sub-centimeter spatial resolution hyperspectral data. Remote Sens. Environ. 298, 113810 https://doi.org/10.1016/j.rse.2023.113810.
Janoutová, R., Homolová, L., Malenovskỳ, Z., Hanuš, J., Lauret, N., Gastellu-Etchegorry, J.P., 2019. Influence of 3D spruce tree representation on accuracy of airborne and satellite forest reflectance simulated in DART. Forests 10, 292. https://doi.org/10.3390/f10030292.
Junttila, S., Ardö, J., Cai, Z., Jin, H., Kljun, N., Klemedtsson, L., Krasnova, A., Lange, H., Lindroth, A., Mölder, M., Noe, S.M., Tagesson, T., Vestin, P., Weslien, P., Eklundh, L., 2023. Estimating local-scale forest GPP in northern Europe using Sentinel-2: model comparisons with LUE, APAR, the plant phenology index, and a light response function. Sci. Remote Sens. 7, 100075 https://doi.org/10.1016/j.srs.2022.100075.
Kazhdan, M., 2021. Screened Poisson Surface Reconstruction (version 8.0). Retrieved from: https://github.com/mkazhdan/PoissonRecon.
Kazhdan, M., Hoppe, H., 2013. Screened poisson surface reconstruction. ACM Trans. Graph. 32 https://doi.org/10.1145/2487228.2487237.
Kükenbrink, D., Hueni, A., Schneider, F.D., Damm, A., Gastellu-Etchegorry, J.P., Schaepman, M.E., Morsdorf, F., 2019. Mapping the irradiance field of a single tree: quantifying vegetation-induced adjacency effects. IEEE Trans. Geosci. Remote Sens. 57, 4994–5011. https://doi.org/10.1109/tgrs.2019.2895211.
Kükenbrink, D., Schneider, F.D., Schmid, B., Gastellu-Etchegorry, J.-P., Schaepman, M. E., Morsdorf, F., 2021. Modelling of three-dimensional, diurnal light extinction in two contrasting forests. Agric. For. Meteorol. 296, 108230 https://doi.org/10.1016/j.agrformet.2020.108230.
Lalic, B., Mihailovic, D.T., 2004. An empirical relation describing leaf-area density inside the forest for environmental modeling. J. Appl. Meteorol. 43, 641–645. https://doi.org/10.1175/1520-0450(2004)043<0641:AERDLD>2.0.CO;2.
Lalic, B., Firanj, A., Mihailovic, D.T., Podrascanin, Z., 2013. Parameterization of PAR vertical profile within horizontally uniform forest canopies for use in environmental modeling. J. Geophys. Res. Atmos. 118, 8156–8165. https://doi.org/10.1002/jgrd.50626.
Lau, A., Bentley, L.P., Martius, C., Shenkin, A., Bartholomeus, H., Raumonen, P., Malhi, Y., Jackson, T., Herold, M., 2018. Quantifying branch architecture of tropical trees using terrestrial LiDAR and 3D modelling. Trees 32, 1219–1231. https://doi.org/10.1007/s00468-018-1704-1.
Laurent, V.C.E., Verhoef, W., Clevers, J.G.P.W., Schaepman, M.E., 2011a. Inversion of a coupled canopy–atmosphere model using multi-angular top-of-atmosphere radiance data: a forest case study. Remote Sens. Environ. 115, 2603–2612. https://doi.org/10.1016/j.rse.2011.05.016.
Laurent, V.C.E., Verhoef, W., Clevers, J.G.P.W., Schaepman, M.E., 2011b. Estimating forest variables from top-of-atmosphere radiance satellite measurements using coupled radiative transfer models. Remote Sens. Environ. 115, 1043–1052. https://doi.org/10.1016/j.rse.2010.12.009.
Laurent, V.C.E., Verhoef, W., Damm, A., Schaepman, M.E., Clevers, J.G.P.W., 2013. A Bayesian object-based approach for estimating vegetation biophysical and biochemical variables from APEX at-sensor radiance data. Remote Sens. Environ. 139, 6–17. https://doi.org/10.1016/j.rse.2013.07.032.
Leblanc, S.G., Chen, J.M., Cihlar, J., 1997. NDVI directionality in boreal forests: a model interpretation of measurements. Can. J. Remote. Sens. 23, 369–380. https://doi.org/10.1080/07038992.1997.10855222.
Lhotáková, Z., Kopačková-Strnadová, V., Oulehle, F., Homolová, L., Neuwirthová, E., Švik, M., Janoutová, R., Albrechtová, J., 2021. Foliage biophysical trait prediction from laboratory spectra in Norway spruce is more affected by needle age than by site soil conditions. Remote Sens. 13, 1–24. https://doi.org/10.3390/rs13030391.
Lin, S., Li, J., Liu, Q., Huete, A., Li, L., 2018. Effects of forest canopy vertical stratification on the estimation of gross primary production by remote sensing. Remote Sens. 10, 1329. https://doi.org/10.3390/rs10091329.
Liu, J., Miller, J.R., Pattey, E., Haboudane, D., Strachan, I.B., Hinther, M., 2004. Monitoring crop biomass accumulation using multi-temporal hyperspectral remote sensing data. In: Igarss 2004 2004 Ieee Int Geoscience Remote Sens Symposium, 3, pp. 1637–1640. https://doi.org/10.1109/igarss.2004.1370643.
Liu, J., Skidmore, A.K., Wang, T., Zhu, X., Premier, J., Heurich, M., Beudert, B., Jones, S., 2019. Variation of leaf angle distribution quantified by terrestrial LiDAR in natural European beech forest. ISPRS J. Photogramm. Remote Sens. 148, 208–220. https://doi.org/10.1016/j.isprsjprs.2019.01.005.
Lukeš, P., Neuwirthová, E., Lhotáková, Z., Janoutová, R., Albrechtová, J., 2020. Upscaling seasonal phenological course of leaf dorsiventral reflectance in radiative transfer model. Remote Sens. Environ. 246, 111862 https://doi.org/10.1016/j.rse.2020.111862.
Malenovský, Z., Martin, E., Homolová, L., Gastellu-Etchegorry, J.P., Zurita-Milla, R., Schaepman, M.E., Pokorný, R., Clevers, J.G.P.W., Cudlín, P., 2008. Influence of woody elements of a Norway spruce canopy on nadir reflectance simulated by the DART model at very high spatial resolution. Remote Sens. Environ. 112, 1–18. https://doi.org/10.1016/j.rse.2006.02.028.
Mkaouar, A., Kallel, A., Rabah, B., Chahed, T.S., Rabah, Z.B., Sahli, T., 2021. Joint estimation of leaf area density and leaf angle distribution using TLS point cloud for forest stands. IEEE J. Sel. Top. Appl. 14, 11095. https://doi.org/10.1109/jstars.2021.3120521.
Morsdorf, F., Nichol, C., Malthus, T., Woodhouse, I.H., 2009. Assessing forest structural and physiological information content of multi-spectral LiDAR waveforms by radiative transfer modelling. Remote Sens. Environ. 113, 2152–2163. https://doi.org/10.1016/j.rse.2009.05.019.
Morsdorf, F., Eck, C., Zgraggen, C., Imbach, B., Schneider, F.D., Kükenbrink, D., 2017. UAV-based LiDAR acquisition for the derivation of high-resolution forest and ground information. Lead. Edge 36, 566–570. https://doi.org/10.1190/tle36070566.1.
Morsdorf, F., Schneider, F.D., Gullien, C., Kükenbrink, D., Leiterer, R., Schaepman, M.E., 2020. Remote Sensing of Plant Biodiversity, pp. 83–104. https://doi.org/10.1007/978-3-030-33157-3_4.
Nunes, M.H., Camargo, J.L.C., Vincent, G., Calders, K., Oliveira, R.S., Huete, A., de Moura, Y.M., Nelson, B., Smith, M.N., Stark, S.C., Maeda, E.E., 2022. Forest fragmentation impacts the seasonality of Amazonian evergreen canopies. Nat. Commun. 13, 1–10. https://doi.org/10.1038/s41467-022-28490-7.
Ollinger, S.V., 2011. Sources of variability in canopy reflectance and the convergent properties of plants. New Phytol. 189, 375–394. https://doi.org/10.1111/j.1469-8137.2010.03536.x.
Paul-Limoges, E., Damm, A., Hueni, A., Liebisch, F., Eugster, W., Schaepman, M.E., Buchmann, N., 2018. Effect of environmental conditions on sun-induced fluorescence in a mixed forest and a cropland. Remote Sens. Environ. 219, 310–323. https://doi.org/10.1016/j.rse.2018.10.018.
Paul-Limoges, E., Wolf, S., Schneider, F.D., Longo, M., Moorcroft, P., Gharun, M., Damm, A., 2020. Partitioning evapotranspiration with concurrent eddy covariance measurements in a mixed forest. Agric. For. Meteorol. 280, 107786 https://doi.org/10.1016/j.agrformet.2019.107786.
Roussel, J.R., Auty, D., Coops, N.C., Tompalski, P., Goodbody, T.R.H., Meador, A.S., Bourdon, J.F., de Boissieu, F., Achim, A., 2020. lidR: an R package for analysis of airborne laser scanning (ALS) data. Remote Sens. Environ. 251, 112061 https://doi.org/10.1016/j.rse.2020.112061.
Rufenacht, D., Fredembach, C., Susstrunk, S., 2013. Automatic and accurate shadow detection using near-infrared information. IEEE Trans. Pattern Anal. Mach. Intell. 36, 1672–1678. https://doi.org/10.1109/tpami.2013.229.
CloudCompare (version 2.12 alpha), [GPL software], 2021, Retrieved from: http://www.cloudcompare.org/.
Running, S.W., Mu, Q., Zhao, M., Moreno, A., 2019. User's Guide MODIS Global Terrestrial Evapotranspiration (ET) Product (MOD16A2/A3 and Year-end Gap-filled MOD16A2GF/A3GF) NASA Earth Observing System MODIS Land Algorithm (For Collection 6). Retrieved from: https://modis-land.gsfc.nasa.gov/pdf/MOD16UsersGuideV2.022019.pdf.
Schaepman-Strub, G., Schaepman, M.E., Painter, T.H., Dangel, S., Martonchik, J.V., 2006. Reflectance quantities in optical remote sensing-definitions and case studies. Remote Sens. Environ. 103, 27–42. https://doi.org/10.1016/j.rse.2006.03.002.
Schnabel, R., Wahl, R., Klein, R., 2007. Efficient RANSAC for point-cloud shape detection. Comput. Graph. Forum 26, 214–226. https://doi.org/10.1111/j.1467-8659.2007.01016.x.
Schneider, F.D., Leiterer, R., Morsdorf, F., Gastellu-Etchegorry, J.P., Lauret, N., Pfeifer, N., Schaepman, M.E., 2014. Simulating imaging spectrometer data: 3D forest modeling based on LiDAR and in situ data. Remote Sens. Environ. 152, 235–250. https://doi.org/10.1016/j.rse.2014.06.015.
Schraik, D., Hovi, A., Rautiainen, M., 2021. Crown level clumping in Norway spruce from terrestrial laser scanning measurements. Agric. For. Meteorol. 296, 108238 https://doi.org/10.1016/j.agrformet.2020.108238.
Schraik, D., Wang, D., Hovi, A., Rautiainen, M., 2023. Quantifying stand-level clumping of boreal, hemiboreal and temperate European forest stands using terrestrial laser scanning. Agric. For. Meteorol. 339, 109564 https://doi.org/10.1016/j.agrformet.2023.109564.
Schunke, S., Leroy, V., Govaerts, Y., 2023. Retrieving BRDFs from UAV-based radiometers for fiducial reference measurements: caveats and recommendations. Front. Remote Sens. 4, 1285800. https://doi.org/10.3389/frsen.2023.1285800.
Siegmann, B., Alonso, L., Celesti, M., Cogliati, S., Colombo, R., Damm, A., Douglas, S., Guanter, L., Hanuš, J., Kataja, K., Kraska, T., Matveeva, M., Moreno, J., Muller, O., Pikl, M., Pinto, F., Vargas, J.Q., Rademske, P., Rodriguez-Morene, F., Sabater, N., Schickling, A., Schüttemeyer, D., Zemek, F., Rascher, U., 2019. The high-performance airborne imaging spectrometer HyPlant-from raw images to top-of-canopy reflectance and fluorescence products: introduction of an automatized processing chain. Remote Sens. 11, 2760. https://doi.org/10.3390/rs11232760.
Siegmann, B., Cendrero-Mateo, M.P., Cogliati, S., Damm, A., Gamon, J., Herrera, D., Jedmowski, C., Junker-Frohn, L.V., Kraska, T., Muller, O., Rademske, P., van der Tol, C., Quiros-Vargas, J., Yang, P., Rascher, U., 2021. Downscaling of far-red solar-induced chlorophyll fluorescence of different crops from canopy to leaf level using a diurnal data set acquired by the airborne imaging spectrometer HyPlant. Remote Sens. Environ. 264, 112609 https://doi.org/10.1016/j.rse.2021.112609.
Sprintsin, M., Chen, J.M., Desai, A., Gough, C.M., 2012. Evaluation of leaf-to-canopy upscaling methodologies against carbon flux data in North America. J. Geophys. Res. Biogeosci. 117 https://doi.org/10.1029/2010jg001407.

Staudt, K., Serafimovich, A., Siebicke, L., Pyles, R.D., Falge, E., 2011. Vertical structure of evapotranspiration at a forest site (a case study). Agric. For. Meteorol. 151, 709–729. https://doi.org/10.1016/j.agrformet.2010.10.009.

Tenhunen, J.D., Valentini, R., Köstner, B., Zimmermann, R., Granier, A., 1998. Variation in forest gas exchange at landscape to continental scales. Annales des Sciences Forestieres 55, 1–11. https://doi.org/10.1051/forest:19980101.

Vincent, G., Antin, C., Laurans, M., Heurtebize, J., Durrieu, S., Lavalley, C., Dauzat, J., 2017. Mapping plant area index of tropical evergreen forest by airborne laser scanning. A cross-validation study using LAI2200 optical sensor. Remote Sens. Environ. 198, 254–266. https://doi.org/10.1016/j.rse.2017.05.034.

Wang, Y., Frankenberg, C., 2022. On the impact of canopy model complexity on simulated carbon, water, and solar-induced chlorophyll fluorescence fluxes. Biogeosciences 19, 29–45. https://doi.org/10.5194/bg-19-29-2022.

Wang, D., Takoudjou, S.M., Casella, E., 2020. LeWoS: a universal leaf-wood classification method to facilitate the 3D modelling of large tropical trees using terrestrial LiDAR. Methods Ecol. Evol. 11, 376–389. https://doi.org/10.1111/2041-210x.13342.

Wei, S., Yi, C., Fang, W., Hendrey, G., 2017. A global study of GPP focusing on light-use efficiency in a random forest regression model. Ecosphere 8, e01724. https://doi.org/10.1002/ecs2.1724.

Widlowski, J.-L., Pinty, B., Lavergne, T., Verstraete, M.M., Gobron, N., 2006. Horizontal radiation transport in 3-D forest canopies at multiple spatial resolutions: simulated impact on canopy absorption. Remote Sens. Environ. 103, 379–397. https://doi.org/10.1016/j.rse.2006.03.014.

Widlowski, J.L., Mio, C., Disney, M., Adams, J., Andredakis, I., Atzberger, C., Brennan, J., Busetto, L., Chelle, M., Ceccherini, G., Colombo, R., Côté, J.F., Eenmäe, A., Essery, R., Gastellu-Etchegorry, J.P., Gobron, N., Grau, E., Haverd, V., Homolová, L., Huang, H., Hunt, L., Kobayashi, H., Koetz, B., Kuusk, A., Kuusk, J., Lang, M., Lewis, P.E., Lovell, J.L., Malenovský, Z., Meroni, M., Morsdorf, F., Mõttus, M., Ni-Meister, W., Pinty, B., Rautiainen, M., Schlerf, M., Somers, B., Stuckens, J., Verstraete, M.M., Yang, W., Zhao, F., Zenone, T., 2015. The fourth phase of the radiative transfer model intercomparison (RAMI) exercise: actual canopy scenarios and conformity testing. Remote Sens. Environ. 169, 418–437. https://doi.org/10.1016/j.rse.2015.08.016.

Zeng, Y., Hao, D., Park, T., Zhu, P., Huete, A., Myneni, R., Knyazikhin, Y., Qi, J., Nemani, R.R., Li, F., Huang, J., Gao, Y., Li, B., Ji, F., Köhler, P., Frankenberg, C., Berry, J.A., Chen, M., 2023. Structural complexity biases vegetation greenness measures. Nat. Ecol. Evol. 1–9. https://doi.org/10.1038/s41559-023-02187-6.

Zhang, K., Kimball, J.S., Running, S.W., 2016. A review of remote sensing based actual evapotranspiration estimation. Wiley Interdiscip. Rev. Water 3, 834–853. https://doi.org/10.1002/wat2.1168.